

A level-set adjoint-state method for crosswell transmission-reflection traveltime tomography

Wenbin Li,¹ Shingyu Leung¹ and Jianliang Qian²

¹*Department of Mathematics, the Hong Kong University of Science and Technology, Clear Water Bay, Hong Kong. E-mail: lwb@ust.hk*

²*Department of Mathematics, Michigan State University, East Lansing, MI 48824, USA*

Accepted 2014 July 5. Received 2014 June 18; in original form 2013 November 25

SUMMARY

We propose a level-set adjoint-state method for crosswell traveltime tomography using both first-arrival transmission and reflection traveltime data. Since our entire formulation is based on solving eikonal and advection equations on finite-difference meshes, our traveltime tomography strategy is carried out without computing rays explicitly. We incorporate reflection traveltime data into the formulation so that possible reflectors (slowness interfaces) in the targeted subsurface model can be recovered as well as the slowness distribution itself. Since a reflector may assume a variety of irregular geometries, we propose to use a level-set function to implicitly parametrize the shape of a reflector. Therefore, a mismatch functional is established to minimize the traveltime data misfit with respect to both the slowness distribution and the level-set function, and the minimization is achieved by using a gradient descent method with gradients computed by solving adjoint state equations. To assess uncertainty or reliability of reconstructed slowness models, we introduce a labelling function to characterize first-arrival ray coverage of the computational domain, and this labelling function satisfies an advection equation. We apply fast-sweeping type methods to solve eikonal, adjoint-state and advection equations arising in our formulation. Numerical examples demonstrate that the proposed algorithm is robust to noise in the measurements, and can recover complicated structure even with little information on the reflector.

Key words: Numerical solutions; Tomography; Non-linear differential equations.

1 INTRODUCTION

Seismic traveltime tomography has been a valuable tool in seismology since the works by Bois *et al.* (1972) and Aki & Lee (1976). Although the concept of traveltime tomography was originally appeared in medical sciences, the inversion of seismic traveltime data dates back to the work of Herglotz and Wiechert as early as 1900s (Aki & Richards 1980). Nowadays seismologists routinely apply tomography to many experimental geometries and different types of data (such as reflection, refraction, transmission and earthquake data) in both crosswell and reflection seismic problems (Bishop *et al.* 1985; McMechan *et al.* 1987; Lutter *et al.* 1990; Zelt & Smith 1992; Delprat-Jannaud & Lailly 1993, 1995; Sei & Symes 1994, 1995; McCaughey & Singh 1997; Zelt 1999; Clarke *et al.* 2001; Rawlinson *et al.* 2001; Washbourne *et al.* 2002; Hobro *et al.* 2003; Montelli *et al.* 2004; Leung & Qian 2005, 2006, 2007; Taillandier *et al.* 2009; Huang *et al.* 2012). In this work, we propose a level-set adjoint-state method for crosswell traveltime tomography using both transmission and reflection data.

In the reflection seismic problems, refraction and wide-angle reflection traveltime tomography is aimed at either simultaneously

determining velocity and interface or determining velocity only by using wide-aperture seismic data (Bishop *et al.* 1985; Kennett *et al.* 1988; Lutter *et al.* 1990; Zelt & Smith 1992; Jurado *et al.* 1996; McCaughey & Singh 1997; Zelt 1999; Rawlinson *et al.* 2001; Hobro *et al.* 2003; Jing *et al.* 2007; Huang & Bellefleur 2012; Huang *et al.* 2012). In the crosswell seismic problems, transmission traveltime tomography is usually aimed at recovering slowness distribution only in between wells (McMechan *et al.* 1987; Bregman *et al.* 1989; Ammon & Vidale 1993; Sei & Symes 1994, 1995; Berryman 2000a,b; Leung & Qian 2005, 2006, 2007; Chung *et al.* 2011; Lelievre *et al.* 2011; Li & Leung 2013), and an explicit recovery of slowness interfaces is usually not addressed. However, in a recent work Zheglova *et al.* (2013), a level-set method (Osher & Sethian 1988) is applied to a particular class of crosswell traveltime tomography in terms of recovering a sharp boundary between two known slowness values from first-arrival transmission data, and mathematically the assumption of known slowness values reduces the inverse problem to a shape optimization problem. Since those sharp boundaries are interfaces of slowness discontinuities which in turn can be viewed as reflectors depending on incident waves, the question is: ‘whether it is possible to

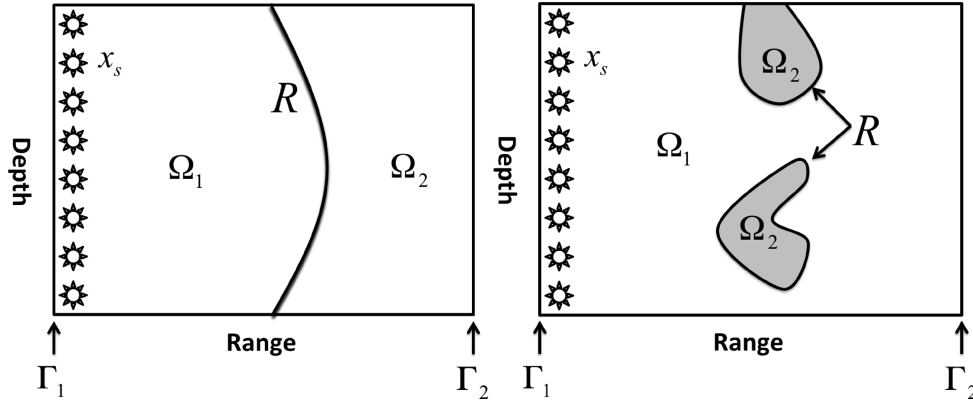


Figure 1. Problem setup.

simultaneously recover slowness distributions and interfaces (reflectors) in crosswell travelt ime tomography?’ (Bube *et al.* 1995) found that from reflection travelt ime inversion, the depths of the reflectors can be better determined than the velocity field in theory, and results of refraction and wide-angle reflection tomography in Farra & Madariaga (1988), White (1989), Lutter *et al.* (1990), Williamson (1990), Zelt & Smith (1992), McCaughey & Singh (1997), Zelt (1999), Rawlinson *et al.* (2001), Hobro *et al.* (2003), Jing *et al.* (2007) and Huang *et al.* (2012) all support that performing a joint tomographic inversion of refraction and reflection data can better constrain slowness as well as reflector geometry. Therefore, we propose to perform a joint tomographic inversion of transmission and reflection data to recover both slowness distributions and slowness interfaces in terms of reflectors in crosswell travelt ime tomography.

Our approach includes several new developments:

(1) Our entire formulation is based on solving eikonal and advection equations by using unconditionally convergent fast-sweeping type schemes on finite-difference meshes (Tsai *et al.* 2003; Kao *et al.* 2004; Zhao 2005; Leung & Qian 2006; Qian *et al.* 2007a,b; Kao *et al.* 2008; Luo *et al.* 2012, 2014) so that the joint crosswell travelt ime tomography is carried out without computing rays explicitly.

(2) Since slowness interfaces can assume a variety of irregular shapes, we use a level-set function defined everywhere to implicitly parametrize those interfaces, and this level-set function is updated by solving an eikonal equation so that possible topological changes of updated interfaces defined by the zero level set can be automatically taken care of during non-linear iterative process.

(3) We establish a mismatch functional to minimize the travelt ime data misfit with respect to the slowness distribution and the level-set function. To apply the gradient descent method to minimize the objective functional, we derive adjoint state equations for computing the gradients of the mismatch functional with respect to the slowness distribution and the level-set function, respectively.

(4) Furthermore, to assess uncertainty or reliability of reconstructed slowness models, we introduce a labelling function to characterize first-arrival ray coverage of the computational domain, and this labelling function can be computed rapidly by solving an advection equation with fast-sweeping type schemes (Leung & Qian 2006).

We carry out some 2-D and 3-D numerical experiments to validate the new formulation.

2 PROBLEM STATEMENT

The problem setup is shown in Fig. 1. Let \mathbf{x}_s be the location of a point source. R is an unknown interface (a possible reflector) which separates the region Ω_2 from Ω_1 . We are interested in the slowness distribution $S(\mathbf{x})$ in the whole region $\Omega = \Omega_1 \cup \Omega_2$. In this work, we assume that the slowness $S(\mathbf{x})$ is piecewise continuous: $S(\mathbf{x}) = S_1(\mathbf{x})$ for $\mathbf{x} \in \Omega_1$, $S(\mathbf{x}) = S_2(\mathbf{x})$ for $\mathbf{x} \in \Omega_2$, $S_1(\mathbf{x}) \in C(\Omega_1)$ and $S_2(\mathbf{x}) \in C(\Omega_2)$.

The transmission travelt ime $T_t(\mathbf{x})$ is given by the following eikonal equation,

$$|\nabla T_t(\mathbf{x})| = S(\mathbf{x}), \quad \mathbf{x} \in \Omega \setminus \{\mathbf{x}_s\} \quad (1)$$

$$T_t(\mathbf{x}) = 0, \quad \mathbf{x} = \mathbf{x}_s; \quad (2)$$

the reflection travelt ime $T_r(\mathbf{x})$ is computed by solving

$$|\nabla T_r(\mathbf{x})| = S(\mathbf{x}), \quad \mathbf{x} \in \Omega_1 \quad (3)$$

$$T_r(\mathbf{x}) = T_t(\mathbf{x}), \quad \mathbf{x} \text{ on } R, \quad (4)$$

where the boundary condition is specified on the interface so that $T_r(\mathbf{x})$ corresponds to the travelt ime of the first reflection.

We have receivers on Γ_2 to record the transmission travelt ime T_t and receivers on Γ_1 to record the reflection travelt ime T_r . The crosswell travelt ime tomography problem reads as follows: given $T_t(\mathbf{x})$ on Γ_2 , $T_r(\mathbf{x})$ on Γ_1 , and the location of point sources $\mathbf{x}_s \in \Omega$, one inverts for the slowness distribution $S(\mathbf{x})$ and the location of the reflector R .

3 THE LEVEL-SET ADJOINT-STATE METHOD

We apply the level-set adjoint-state method (Li & Leung 2013) to solve this tomography problem. The adjoint-state method formulates the inverse problem as the minimization of a mismatch functional under constraint of partial differential equations, and it evaluates the gradient of the mismatch functional by solving a system of adjoint-state equations.

In our problem, the mismatch functional is given by

$$E(S) = \frac{1}{2} \int_{\Gamma_1} |T_r - T_r^*|^2 ds + \frac{1}{2} \int_{\Gamma_2} |T_t - T_t^*|^2 ds, \quad (5)$$

where T_t^* corresponds to first-arrival travelt imes of the transmitted waves measured on Γ_2 , T_r^* corresponds to first-arrival travelt imes measured on Γ_1 of the reflected waves starting from the reflector.

T_t and T_r are the corresponding viscosity solutions of eqs (1)–(2) and eqs (3)–(4), respectively. Our goal is to minimize this mismatch functional to find a suitable slowness distribution $S(\mathbf{x})$.

3.1 Level-set parametrization and slowness perturbation

Since we are concerned with a piecewise continuous slowness model separated by an interface, we use a level-set function to express such a structure:

$$S(\mathbf{x}) = S_1(\mathbf{x}) \cdot \{1 - H[\phi(\mathbf{x})]\} + S_2(\mathbf{x}) \cdot H[\phi(\mathbf{x})].$$

Here the level set function $\phi(\mathbf{x})$ is the signed distance to the interface R ,

$$\phi(\mathbf{x}) = \begin{cases} -\text{dist}(\mathbf{x}, R), & \mathbf{x} \in \Omega_1, \\ \text{dist}(\mathbf{x}, R), & \mathbf{x} \in \Omega_2, \end{cases}$$

and $H: \mathbb{R} \rightarrow \mathbb{R}$ is the Heaviside function with

$$H(x) = \begin{cases} 0, & x < 0, \\ 1, & x > 0. \end{cases}$$

To recover the original slowness model $S(\mathbf{x})$, we need to invert for $S_1(\mathbf{x})$, $S_2(\mathbf{x})$ and $\phi(\mathbf{x})$ so that the reflector $R = \phi^{-1}(0)$. Since it is a non-linear problem, we use a gradient descent method to minimize the mismatch functional. To study the change of $S(\mathbf{x})$ with respect to perturbations of $\phi(\mathbf{x})$, $S_1(\mathbf{x})$ and $S_2(\mathbf{x})$, we use a smoothed version of the Heaviside function by introducing a small parameter τ ($0 < \tau < 1$),

$$H_\tau(\phi) = \frac{1}{2} \left(\tanh \frac{\phi}{\tau} + 1 \right). \quad (6)$$

Then the slowness is expressed as

$$S(\mathbf{x}) = S_1(\mathbf{x}) \cdot \{1 - H_\tau[\phi(\mathbf{x})]\} + S_2(\mathbf{x}) \cdot H_\tau[\phi(\mathbf{x})], \quad (7)$$

and the perturbation is given by

$$\begin{aligned} & S(\phi + \epsilon\tilde{\phi}, S_1 + \epsilon\tilde{S}_1, S_2 + \epsilon\tilde{S}_2) - S(\phi, S_1, S_2) \\ &= (S_2 - S_1) \cdot [H_\tau(\phi + \epsilon\tilde{\phi}) - H_\tau(\phi)] + \epsilon\tilde{S}_1 \\ & \quad \cdot [1 - H_\tau(\phi + \epsilon\tilde{\phi})] + \epsilon\tilde{S}_2 \cdot H_\tau(\phi + \epsilon\tilde{\phi}). \end{aligned} \quad (8)$$

As shown in Li & Leung (2013), we have

$$\begin{aligned} H_\tau(\phi + \epsilon\tilde{\phi}) - H_\tau(\phi) &= \epsilon\tilde{\phi} \cdot \frac{1}{2\tau \cdot \cosh^2 \frac{\phi}{\tau}} - \epsilon^2 \tilde{\phi}^2 \cdot \frac{\tanh \frac{\xi}{\tau}}{2\tau^2 \cdot \cosh^2 \frac{\xi}{\tau}} \\ &= \begin{cases} O(1), \phi = O(\tau^\alpha) & \text{and } \alpha \geq 1, \\ O(\epsilon), \phi = O(\tau^\alpha) & \text{and } \alpha < 1, \end{cases} \end{aligned} \quad (9)$$

where $\xi \in (\phi, \phi + \epsilon\tilde{\phi})$. Here the notation $f = O(g)$ means that $\exists C > 0$, such that $|f| \leq C|g|$. The order is estimated in the sense of $\tau \rightarrow 0$, and we choose $\epsilon \leq \tau$. Since $\phi = O(\tau^\alpha)$ with $\alpha \geq 1$ only occurs for those \mathbf{x} near the reflector R , the region consisting of those \mathbf{x} is of measure zero in the limit as $\tau \rightarrow 0$. Plugging the formula (9) into (8), we get

$$\begin{aligned} & S(\phi + \epsilon\tilde{\phi}, S_1 + \epsilon\tilde{S}_1, S_2 + \epsilon\tilde{S}_2) - S(\phi, S_1, S_2) \\ &= \begin{cases} O(1), \phi = O(\tau^\alpha) & \text{and } \alpha \geq 1, \\ O(\epsilon), \phi = O(\tau^\alpha) & \text{and } \alpha < 1. \end{cases} \end{aligned} \quad (10)$$

In the following, we derive the corresponding changes δT_t and δT_r in T_t and T_r due to the perturbation of the slowness $S(\mathbf{x})$.

The transmission traveltine $T_t(\mathbf{x})$ depends on the accumulation of the slowness along a ray γ starting from the source \mathbf{x}_s and reaching \mathbf{x} : $\gamma = \{\mathbf{y}(s): 0 \leq s \leq L\}$, where L is the arc length of the underlying ray. Similar to the argument in our previous work Li & Leung (2013), we look at

$$\begin{aligned} T_t(\mathbf{x}) &= \int_\gamma S[\mathbf{y}(s)] ds = \int_{\gamma \cap \{\mathbf{y}: \phi = O(\tau^\alpha), \alpha \geq 1\}} S(s) ds \\ & \quad + \int_{\gamma \cap \{\mathbf{y}: \phi = O(\tau^\alpha), \alpha < 1\}} S(s) ds, \end{aligned} \quad (11)$$

where $S(s) \equiv S(\mathbf{y}(s))$ corresponds to the slowness along the ray γ . Since the measure of the set $\{\mathbf{y}: \phi(\mathbf{y}) = O(\tau^\alpha), \alpha \geq 1\}$ is $O(\tau) = O(\epsilon)$, we expect that the corresponding change of $T_t(\mathbf{x})$ due to the perturbation in (10) is of $O(\epsilon)$, viz. $\delta T_t = O(\epsilon)$.

The perturbation on the reflection traveltine $T_r(\mathbf{x})$ is more complicated. Looking at (3) and (4), one finds that several parameters affect the solution $T_r(\mathbf{x})$, including the domain Ω_1 , the slowness distribution $S_1(\mathbf{x})$ in Ω_1 , the location of the reflector R , and the values of $T_r(\mathbf{x})$ on R . All these related parameters will be affected once we perturb $S(\phi, S_1, S_2)$ in (10), and the change of Ω_1 (and therefore the boundary location R) usually introduces abrupt changes to the solution $T_r(\mathbf{x})$ (McCaughy & Singh 1997). To obtain a smooth change in successive iterations, we first imagine that we perturb only S_1 and S_2 by fixing ϕ to get $S(\phi, S_1 + \epsilon\tilde{S}_1, S_2 + \epsilon\tilde{S}_2)$ so that the domain of $T_r(\mathbf{x})$, Ω_1 , and the boundary R are frozen; consequently, δT_r is only related to the perturbation of $S(\mathbf{x})$ in Ω_1 and the change of $T_r(\mathbf{x})$ on R . Since we already know that $\delta T_r(\mathbf{x}) = O(\epsilon)$ and the perturbation of $S(\mathbf{x})$ is depicted by (10), using the same argument as for $T_t(\mathbf{x})$ we can deduce that the corresponding perturbation on $T_r(\mathbf{x})$ is of $O(\epsilon)$. In practice of course we cannot have ϕ frozen since we have to invert for the location of the reflector; however, the above consideration inspires us that we can reduce the perturbation on ϕ to control the magnitude of δT_r . Since ϕ and S have different dimensions, we introduce another small parameter ν ($0 < \nu < 1$) to $\tilde{\phi}$ and use $\nu\tilde{\phi}$ as the perturbation parameter in the level set function. Since $\delta S = S(\phi + \epsilon \cdot \nu\tilde{\phi}, S_1 + \epsilon\tilde{S}_1, S_2 + \epsilon\tilde{S}_2) - S(\phi, S_1, S_2)$, we expect that the change in Ω_1 (and so the change in R) is very small. Thus the relation $\delta T_r(\mathbf{x}) = O(\epsilon)$ holds almost everywhere in Ω_1 .

In summary, with the perturbation of the slowness

$$\delta S = S(\phi + \epsilon \cdot \nu\tilde{\phi}, S_1 + \epsilon\tilde{S}_1, S_2 + \epsilon\tilde{S}_2) - S(\phi, S_1, S_2), \quad (12)$$

we expect that the corresponding perturbation on the traveltine is in the form of

$$\begin{aligned} & T_t(\phi + \epsilon \cdot \nu\tilde{\phi}, S_1 + \epsilon\tilde{S}_1, S_2 + \epsilon\tilde{S}_2) \\ & \quad - T_t(\phi, S_1, S_2) = \epsilon \cdot \tilde{T}_t \quad a.e. \text{ in } \Omega, \end{aligned} \quad (13)$$

$$\begin{aligned} & T_r(\phi + \epsilon \cdot \nu\tilde{\phi}, S_1 + \epsilon\tilde{S}_1, S_2 + \epsilon\tilde{S}_2) \\ & \quad - T_r(\phi, S_1, S_2) = \epsilon \cdot \tilde{T}_r \quad a.e. \text{ in } \Omega_1, \end{aligned} \quad (14)$$

where *a.e.* denotes ‘almost everywhere’.

Then combining (13) and (14) with the eikonal eq. (1), we can derive the following formulas directly relating $\tilde{\phi}$, \tilde{S}_1 , \tilde{S}_2 , \tilde{T}_t and \tilde{T}_r by following (Li & Leung 2013) with detailed calculation given in Appendix A:

$$\begin{aligned} & \nu\tilde{\phi} \cdot A(\phi, S_1, S_2) + \tilde{S}_1 \cdot B(\phi, S_1, S_2) + \tilde{S}_2 \cdot C(\phi, S_1, S_2) \\ & \quad - \nabla T_t \cdot \nabla \tilde{T}_t = 0 \quad a.e. \text{ in } \Omega \end{aligned} \quad (15)$$

$$\begin{aligned} v\tilde{\phi} \cdot A(\phi, S_1, S_2) + \tilde{S}_1 \cdot B(\phi, S_1, S_2) + \tilde{S}_2 \cdot C(\phi, S_1, S_2) \\ - \nabla T_r \cdot \nabla \tilde{T}_r = 0, \quad a.e. \text{ in } \Omega_1, \end{aligned} \quad (16)$$

where

$$A(\phi, S_1, S_2) = S(\phi, S_1, S_2) \cdot \frac{S_2 - S_1}{2\tau \cdot \cosh^2 \frac{\phi}{\tau}}, \quad (17)$$

$$B(\phi, S_1, S_2) = S(\phi, S_1, S_2) \cdot [1 - H_\tau(\phi)], \quad (18)$$

$$C(\phi, S_1, S_2) = S(\phi, S_1, S_2) \cdot H_\tau(\phi). \quad (19)$$

3.2 Adjoint-state method for the gradient

Now we use the adjoint-state method to calculate the gradient-descent direction of the mismatch functional. With (5), (13) and (14), the perturbation on the mismatch functional is given by

$$\begin{aligned} \delta E / \epsilon = [E(\phi + \epsilon \cdot v\tilde{\phi}, S_1 + \epsilon\tilde{S}_1, S_2 + \epsilon\tilde{S}_2) - E(\phi, S_1, S_2)] / \epsilon \\ = \int_{\Gamma_1} \tilde{T}_r(T_r - T_r^*) ds + \int_{\Gamma_2} \tilde{T}_r(T_r - T_r^*) ds + O(\epsilon). \end{aligned} \quad (20)$$

We will eliminate the dependence of (20) on \tilde{T}_r and \tilde{T}_r by introducing adjoint state equations. To simplify the notation, we denote

$$W = v\tilde{\phi} \cdot A(\phi, S_1, S_2) + \tilde{S}_1 \cdot B(\phi, S_1, S_2) + \tilde{S}_2 \cdot C(\phi, S_1, S_2), \quad (21)$$

where A , B and C are given by eqs (17)–(19). We have the following results.

Lemma 3.1. If λ satisfies the adjoint state equation

$$-\operatorname{div}(\lambda \nabla T_r) = 0 \quad \text{in } \Omega, \quad (22)$$

$$\lambda \frac{\partial T_r}{\partial \mathbf{n}} = T_r - T_r^* \quad \text{on } \Gamma_2, \quad (23)$$

$$\lambda = 0 \quad \text{on } \partial\Omega \setminus \Gamma_2, \quad (24)$$

where \mathbf{n} denotes the unit outward normal of $\partial\Omega$, then (20) is reduced to

$$\frac{\delta E}{\epsilon} = \int_{\Omega} \lambda W \, d\mathbf{x} + \int_{\Gamma_1} \tilde{T}_r(T_r - T_r^*) ds + O(\epsilon). \quad (25)$$

Lemma 3.2. If μ satisfies the adjoint state equation

$$-\operatorname{div}(\mu \nabla T_r) = 0 \quad \text{in } \Omega_1, \quad (26)$$

$$\mu \frac{\partial T_r}{\partial \mathbf{n}} = T_r - T_r^* \quad \text{on } \Gamma_1, \quad (27)$$

$$\mu = 0 \quad \text{on } \partial\Omega_1 \setminus (R \cup \Gamma_1), \quad (28)$$

and $\hat{\mu}$ satisfies the adjoint state equation

$$-\operatorname{div}(\hat{\mu} \nabla T_r) = 0 \quad \text{in } \Omega_1, \quad (29)$$

$$\hat{\mu} = \mu \quad \text{on } R, \quad (30)$$

$$\hat{\mu} = 0 \quad \text{on } \partial\Omega_1 \setminus R, \quad (31)$$

then the perturbation of the mismatch functional is reduced to

$$\frac{\delta E}{\epsilon} = \int_{\Omega} \lambda W \, d\mathbf{x} + \int_{\Omega_1} (\mu + \hat{\mu}) W \, d\mathbf{x} + O(\epsilon). \quad (32)$$

We give the detailed proofs of these two lemmas in Appendix B.

Although the adjoint states μ and $\hat{\mu}$ are defined only in Ω_1 , we can extend them to the whole domain Ω by setting

$$\mu(\mathbf{x}) = \begin{cases} \mu(\mathbf{x}) & \text{in } \mathbf{x} \in \Omega_1 \\ 0 & \text{in } \mathbf{x} \in \Omega \setminus \Omega_1, \end{cases} \quad (33)$$

and

$$\hat{\mu}(\mathbf{x}) = \begin{cases} \hat{\mu}(\mathbf{x}) & \text{in } \mathbf{x} \in \Omega_1 \\ 0 & \text{in } \mathbf{x} \in \Omega \setminus \Omega_1. \end{cases} \quad (34)$$

Thus (32) can be rewritten as

$$\frac{\delta E}{\epsilon} = \int_{\Omega} (\lambda + \mu + \hat{\mu}) W \, d\mathbf{x} + O(\epsilon). \quad (35)$$

Using formula (21) and neglecting the $O(\epsilon)$ term in (35), we obtain a descent direction of the perturbation by taking

$$\tilde{\phi} = -A(\phi, S_1, S_2) \cdot (\lambda + \mu + \hat{\mu}), \quad (36)$$

$$\tilde{S}_1 = -B(\phi, S_1, S_2) \cdot (\lambda + \mu + \hat{\mu}), \quad (37)$$

$$\tilde{S}_2 = -C(\phi, S_1, S_2) \cdot (\lambda + \mu + \hat{\mu}), \quad (38)$$

so that we have

$$\delta E \approx -\epsilon \cdot \int_{\Omega} (\lambda + \mu + \hat{\mu})^2 (vA^2 + B^2 + C^2) \, d\mathbf{x} \leq 0.$$

3.3 Regularizations of $\phi(\mathbf{x})$, $S_1(\mathbf{x})$ and $S_2(\mathbf{x})$

For the level set function $\phi(\mathbf{x})$, we use the level set re-initialization to maintain ϕ as a signed distance function as done in Li & Leung (2013). Specifically, we solve the following system in an artificial time direction ξ

$$\frac{\partial \Phi}{\partial \xi} + \operatorname{sign}(\phi) \cdot (|\nabla \Phi| - 1) = 0, \quad (39)$$

$$\Phi(\mathbf{x}, \xi = 0) = \phi(\mathbf{x}), \quad (40)$$

$$\frac{\partial \Phi}{\partial \mathbf{n}} \Big|_{\partial\Omega} = 0, \quad (41)$$

where $\operatorname{sign}(\phi) = \frac{2}{\pi} \arctan \phi$ is the signum function (Qian & Leung 2004). Since we are only interested in the solution near the zero level set, in practice there is no need to get the steady state solution. Evolving this equation for several $\Delta\xi$ steps, we replace the original level set function ϕ with the solution Φ .

To maintain a stable update on the shape of the reflector R in terms of the zero level-set function ϕ , we regularize ϕ to smoothen the shape of the reflector R which is achieved by penalizing the L^2 norm of $\nabla\phi(\mathbf{x})$ so that the new mismatch functional is defined by

$$E_{\text{new}} = E + \gamma \cdot E_{\phi}, \quad (42)$$

where E is given by formula (5), γ is a parameter to control the weight, and E_{ϕ} measures the L^2 norm of $\nabla\phi$ given by

$$E_{\phi} = \frac{1}{2} \int_{\Omega} |\nabla\phi|^2 \, d\mathbf{x}. \quad (43)$$

When the slowness perturbation is given by (12), the corresponding change in E_{ϕ} is

$$\begin{aligned}
\delta E_\phi &= E_\phi(\phi + \epsilon \cdot v\tilde{\phi}) - E_\phi(\phi) \\
&= \epsilon v \cdot \int_\Omega \nabla \phi \cdot \nabla \tilde{\phi} \, d\mathbf{x} + O(\epsilon^2) \\
&= \epsilon v \cdot \left[- \int_\Omega \Delta \phi \cdot \tilde{\phi} \, d\mathbf{x} + \int_{\partial\Omega} \frac{\partial \phi}{\partial \mathbf{n}} \cdot \tilde{\phi} \, ds \right] + O(\epsilon^2). \quad (44)
\end{aligned}$$

In (44), $\phi(\mathbf{x})$ is the level set function before perturbation but after re-initialization. Since we have $\frac{\partial \phi}{\partial \mathbf{n}}|_{\partial\Omega} = 0$ due to (41), (44) leads to

$$\delta E_\phi = -\epsilon v \cdot \int_\Omega \Delta \phi \cdot \tilde{\phi} \, d\mathbf{x} + O(\epsilon^2). \quad (45)$$

Combining (35), (42) and (45), we have

$$\begin{aligned}
\frac{\delta E_{\text{new}}}{\epsilon} &= \frac{\delta E}{\epsilon} + \gamma \cdot \frac{\delta E_\phi}{\epsilon} \\
&= \int_\Omega v\tilde{\phi} \cdot [(\lambda + \mu + \hat{\mu})A(\phi, S_1, S_2) - \gamma \Delta \phi] \, d\mathbf{x} \\
&\quad + \int_\Omega (\lambda + \mu + \hat{\mu}) \cdot (\tilde{S}_1 \cdot B(\phi, S_1, S_2) \\
&\quad + \tilde{S}_2 \cdot C(\phi, S_1, S_2)) \, d\mathbf{x} + O(\epsilon). \quad (46)
\end{aligned}$$

Thus to get the gradient descent of the newly defined mismatch functional E_{new} , the perturbation on ϕ should be modified as

$$\tilde{\phi} = -A(\phi, S_1, S_2) \cdot (\lambda + \mu + \hat{\mu}) + \gamma \Delta \phi, \quad (47)$$

where the term $\gamma \Delta \phi$ provides the regularization to control the shape of the reflector.

We also need to regularize $\tilde{S}_1(\mathbf{x})$ and $\tilde{S}_2(\mathbf{x})$ before updating $S_1(\mathbf{x})$ and $S_2(\mathbf{x})$ during each iteration. With (46), the corresponding change of the mismatch functional due to \tilde{S}_1 is

$$\delta E_{S_1} := \epsilon \cdot \int_\Omega (\lambda + \mu + \hat{\mu}) B(\phi, S_1, S_2) \tilde{S}_1 \, d\mathbf{x}, \quad (48)$$

so that \tilde{S}_1 is selected as in (37) to achieve the gradient descent. Also the corresponding change of the mismatch functional due to \tilde{S}_2 is

$$\delta E_{S_2} := \epsilon \cdot \int_\Omega (\lambda + \mu + \hat{\mu}) C(\phi, S_1, S_2) \tilde{S}_2 \, d\mathbf{x}, \quad (49)$$

so that \tilde{S}_2 is chosen to be the form in (38). We smoothen \tilde{S}_1 and \tilde{S}_2 by solving the following equations,

$$\begin{aligned}
(I - \alpha \Delta) \tilde{S}_1^* &= \tilde{S}_1 = -B(\phi, S_1, S_2) \cdot (\lambda + \mu + \hat{\mu}) & \text{in } \Omega, \\
\frac{\partial \tilde{S}_1^*}{\partial \mathbf{n}} &= 0 & \text{on } \partial\Omega \quad (50)
\end{aligned}$$

and

$$\begin{aligned}
(I - \alpha \Delta) \tilde{S}_2^* &= \tilde{S}_2 = -C(\phi, S_1, S_2) \cdot (\lambda + \mu + \hat{\mu}) & \text{in } \Omega, \\
\frac{\partial \tilde{S}_2^*}{\partial \mathbf{n}} &= 0 & \text{on } \partial\Omega, \quad (51)
\end{aligned}$$

where I is the identity operator, Δ is the Laplace operator, and $\alpha > 0$ is the weight controlling the amount of regularity that one wants. Then we use \tilde{S}_1^* and \tilde{S}_2^* to replace \tilde{S}_1 and \tilde{S}_2 in the perturbation, which leads to

$$\begin{aligned}
\delta E_{S_1} &= \epsilon \cdot \int_\Omega (\lambda + \mu + \hat{\mu}) B(\phi, S_1, S_2) \cdot \tilde{S}_1^* \, d\mathbf{x} \\
&= -\epsilon \cdot \int_\Omega (I - \alpha \Delta) \tilde{S}_1^* \cdot \tilde{S}_1^* \, d\mathbf{x} \\
&= -\epsilon \cdot \int_\Omega [(\tilde{S}_1^*)^2 + \alpha |\nabla \tilde{S}_1^*|^2] \, d\mathbf{x} \leq 0
\end{aligned}$$

and

$$\delta E_{S_2} = -\epsilon \cdot \int_\Omega [(\tilde{S}_2^*)^2 + \alpha |\nabla \tilde{S}_2^*|^2] \, d\mathbf{x} \leq 0.$$

3.4 Formulas for multiple shots

In a typical seismic survey, we collect data sets for multiple shots. We summarize formulas for dealing with multiple point sources. Specifically we denote $\{T_{r,j}|_{\Gamma_2}\}$ and $\{T_{r,j}|_{\Gamma_1}\}$ the data sets corresponding to the point source located at $\mathbf{x}_s^j, j = 1, 2, 3, \dots, N$. We simply sum up all individual mismatch functionals and minimize

$$\begin{aligned}
E^N(\phi, S_1, S_2) &= \frac{1}{2} \sum_{j=1}^N \int_{\Gamma_1} |T_{r,j} - T_{r,j}^*|^2 \, ds \\
&\quad + \frac{1}{2} \sum_{j=1}^N \int_{\Gamma_2} |T_{t,j} - T_{t,j}^*|^2 \, ds + \gamma \cdot \frac{1}{2} \int_\Omega |\nabla \phi|^2 \, d\mathbf{x}, \quad (52)
\end{aligned}$$

where $T_{t,j}$ and $T_{r,j}$ are the solutions to (1)–(2) and (3)–(4), respectively, corresponding to the point source \mathbf{x}_s^j . With almost the same calculation as above, we have the perturbation of E^N ,

$$\begin{aligned}
\frac{\delta E^N}{\epsilon} &= \frac{E^N(\phi + \epsilon v\tilde{\phi}, S_1 + \epsilon \tilde{S}_1, S_2 + \epsilon \tilde{S}_2) - E^N(\phi, S_1, S_2)}{\epsilon} \\
&= \int_\Omega v\tilde{\phi} \cdot \left[\sum_j (\lambda_j + \mu_j + \hat{\mu}_j) A(\phi, S_1, S_2) - \gamma \Delta \phi \right] \, d\mathbf{x} \\
&\quad + \int_\Omega \sum_j (\lambda_j + \mu_j + \hat{\mu}_j) \cdot [\tilde{S}_1 \cdot B(\phi, S_1, S_2) \\
&\quad + \tilde{S}_2 \cdot C(\phi, S_1, S_2)] \, d\mathbf{x} + O(\epsilon) \quad (53)
\end{aligned}$$

where A, B and C are given by formulas (17), (18) and (19). The adjoint states λ_j, μ_j and $\hat{\mu}_j$ are computed by solving the following adjoint state equations:

$$\begin{aligned}
-\operatorname{div}(\lambda_j \nabla T_{t,j}) &= 0 & \text{in } \Omega, \\
\lambda_j \frac{\partial T_{t,j}}{\partial \mathbf{n}} &= T_{t,j} - T_{t,j}^* & \text{on } \Gamma_2, \\
\lambda_j &= 0 & \text{on } \partial\Omega \setminus \Gamma_2, \quad (54)
\end{aligned}$$

$$\begin{aligned}
-\operatorname{div}(\mu_j \nabla T_{r,j}) &= 0 & \text{in } \Omega_1, \\
\mu_j \frac{\partial T_{r,j}}{\partial \mathbf{n}} &= T_{r,j} - T_{r,j}^* & \text{on } \Gamma_1, \\
\mu_j &= 0 & \text{on } \partial\Omega_1 \setminus (R \cup \Gamma_1), \quad (55)
\end{aligned}$$

and

$$\begin{aligned}
-\operatorname{div}(\hat{\mu}_j \nabla T_{t,j}) &= 0 & \text{in } \Omega_1, \\
\hat{\mu}_j &= \mu_j & \text{on } R, \\
\hat{\mu}_j &= 0 & \text{on } \partial\Omega_1 \setminus R, \quad (56)
\end{aligned}$$

and we extend the values of μ_j and $\hat{\mu}_j$ to the whole domain Ω by setting

$$\mu_j = \begin{cases} \mu_j & \text{in } \Omega_1, \\ 0 & \text{in } \Omega \setminus \Omega_1, \end{cases} \quad (57)$$

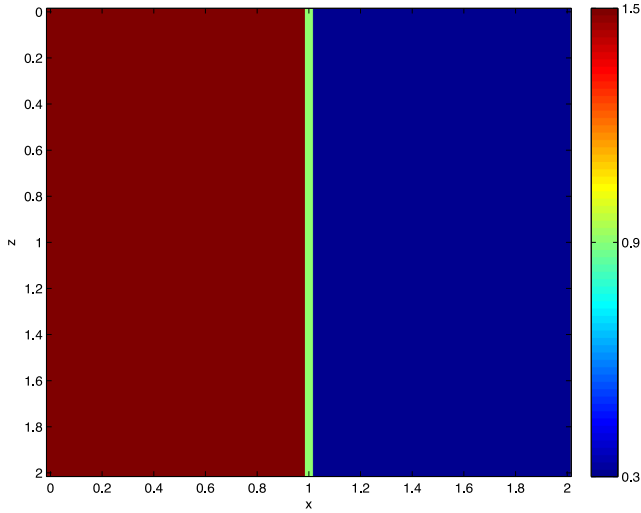


Figure 2. (Example 1): initial guess of $S(\mathbf{x})$.

$$\hat{\mu}_j = \begin{cases} \hat{\mu}_j & \text{in } \Omega_1, \\ 0 & \text{in } \Omega \setminus \Omega_1. \end{cases} \quad (58)$$

To achieve the gradient descent, $\tilde{\phi}$ is set to be

$$\tilde{\phi} = - \sum_j (\lambda_j + \mu_j + \hat{\mu}_j) \cdot A(\phi, S_1, S_2) + \gamma \Delta \phi, \quad (59)$$

while \tilde{S}_1 and \tilde{S}_2 are obtained by solving the following regularization equations:

$$\begin{aligned} (I - \alpha \Delta) \tilde{S}_1 &= -B(\phi, S_1, S_2) \cdot \sum_j (\lambda_j + \mu_j + \hat{\mu}_j) & \text{in } \Omega, \\ \frac{\partial \tilde{S}_1}{\partial \mathbf{n}} &= 0 & \text{on } \partial \Omega, \end{aligned} \quad (60)$$

and

$$\begin{aligned} (I - \alpha \Delta) \tilde{S}_2 &= -C(\phi, S_1, S_2) \cdot \sum_j (\lambda_j + \mu_j + \hat{\mu}_j) & \text{in } \Omega, \\ \frac{\partial \tilde{S}_2}{\partial \mathbf{n}} &= 0 & \text{on } \partial \Omega. \end{aligned} \quad (61)$$

Then the functions $\phi(\mathbf{x})$, $S_1(\mathbf{x})$ and $S_2(\mathbf{x})$ are updated according to

$$\begin{aligned} \phi^{\text{new}}(\mathbf{x}) &= \phi^{\text{old}}(\mathbf{x}) + \epsilon \cdot \nu \tilde{\phi}, \\ S_1^{\text{new}}(\mathbf{x}) &= S_1^{\text{old}}(\mathbf{x}) + \epsilon \cdot \tilde{S}_1, \\ S_2^{\text{new}}(\mathbf{x}) &= S_2^{\text{old}}(\mathbf{x}) + \epsilon \cdot \tilde{S}_2. \end{aligned}$$

Finally, we re-initialize the level set function $\phi(\mathbf{x})$ by solving (39)–(41) and then update the slowness distribution $S(\mathbf{x})$ using formula (7).

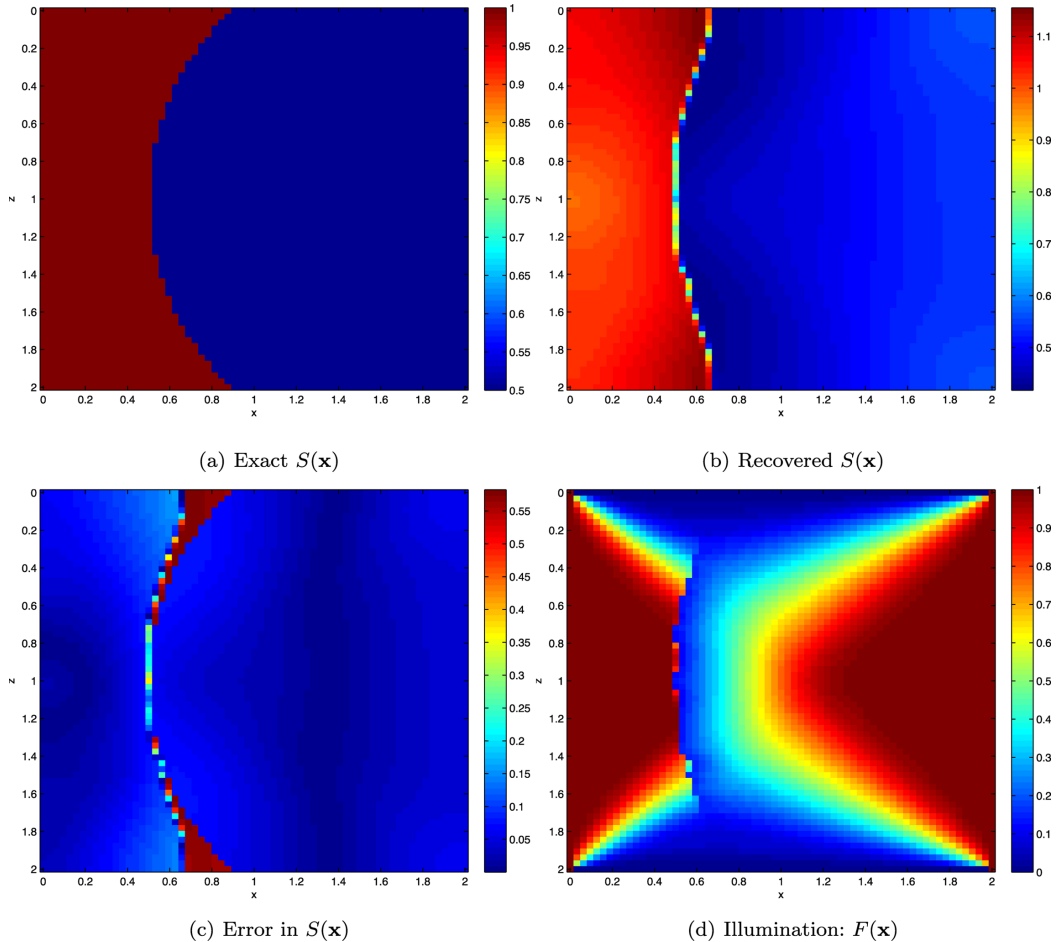


Figure 3. (Example 1, Case 1): piecewise homogeneous structure.

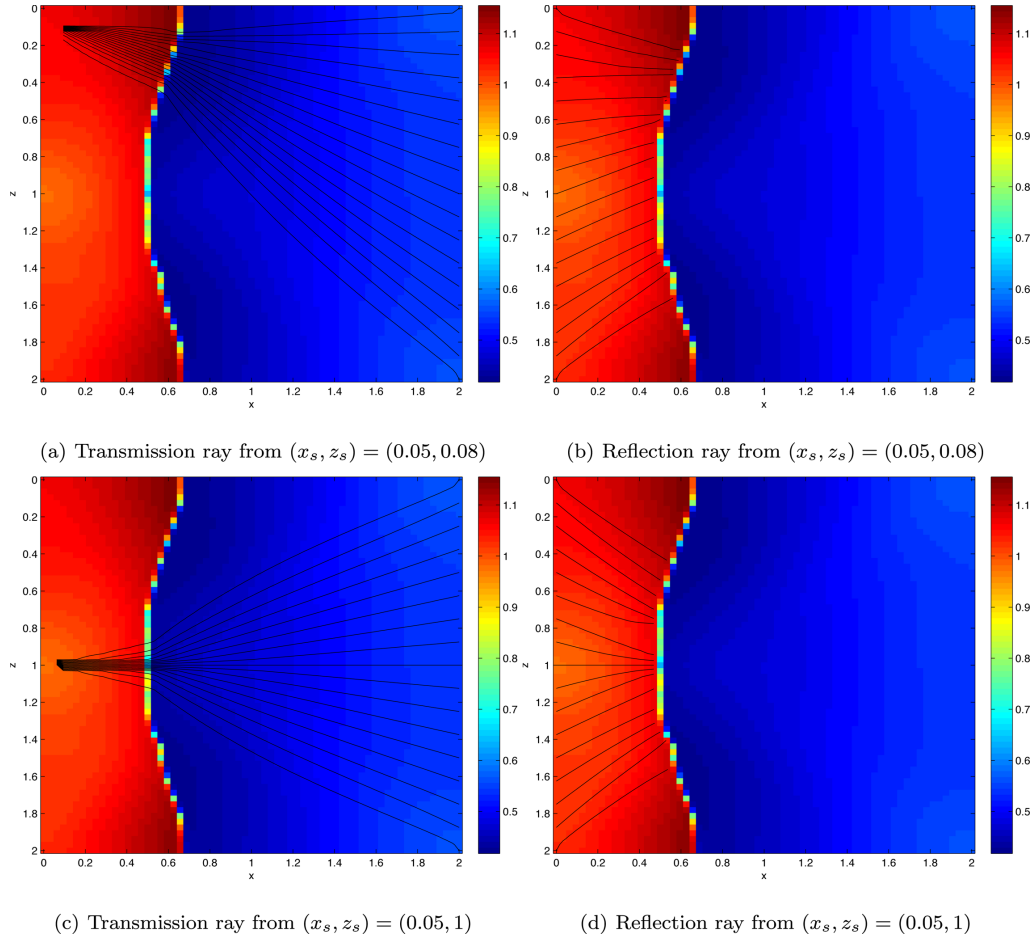


Figure 4. (Example 1, Case 1): Lagrangian ray paths for the illuminated region.

4 INDICATION OF ILLUMINATED AND UNILLUMINATED REGIONS

In this section, we study the reliability of our reconstruction. When a slowness model $S(\mathbf{x})$ is inhomogeneous, it is common to have shadow regions between point sources and receivers; namely, there are no rays passing through certain regions of larger slowness value. The existence of such shadow regions implies potential difficulties for first-arrival based seismic traveltime tomography since the observed first-arrival traveltimes at the boundary receivers are due to detoured rays which avoid these slow regions with large $S(\mathbf{x})$; consequently, we may not be able to recover the slowness in those slow regions. To assess uncertainty or reliability of reconstructed slowness models, we introduce a labelling function to identify those regions where the reconstruction is not reliable. As a result, this labelling function provides a reliability measure for the inversion.

Given a point source, we say that a point is illuminated if there exists a first-arrival ray connecting the source and a receiver such that this ray passes through this point. All such illuminated points define an illuminated region corresponding to the given source point. To compute such an illuminated region, we define a labelling function $F(\mathbf{x})$ such that it has a value 1 if \mathbf{x} is in the illuminated region and it equals 0 otherwise. Consider an arc-length parametrized ray $\{\mathbf{x}: \mathbf{x} = \mathbf{x}(s)\}$ arriving at a receiver \mathbf{x}^* on the boundary. We hope that $F(\mathbf{x}) \equiv 1$ along the ray, or equivalently

$$\frac{dF[\mathbf{x}(s)]}{ds} = 0 \quad (62)$$

which implies

$$\nabla F(\mathbf{x}) \cdot \frac{d\mathbf{x}(s)}{ds} = 0. \quad (63)$$

Since the ray direction from the receiver \mathbf{x}^* to the source \mathbf{x}_s is given by

$$\frac{d\mathbf{x}(s)}{ds} = -\frac{\nabla T(\mathbf{x})}{S(\mathbf{x})}. \quad (64)$$

we have

$$-\nabla F(\mathbf{x}) \cdot \nabla T(\mathbf{x}) = 0, \quad F|_{\Gamma} = 1, \quad (65)$$

where $T(\mathbf{x}) = T(\mathbf{x}; \mathbf{x}_s)$ is the first-arrival traveltime with the source at \mathbf{x}_s , and Γ is the location of boundary receivers.

According to the above consideration, we introduce two labelling functions $F_t(\mathbf{x})$ and $F_r(\mathbf{x})$ for transmission traveltime field $T_t(\mathbf{x}; \mathbf{x}_s)$ and reflection traveltime field $T_r(\mathbf{x}; \mathbf{x}_s)$, respectively,

$$\begin{aligned} -\nabla F_t(\mathbf{x}) \cdot \nabla T_t(\mathbf{x}) &= 0, & \mathbf{x} \in \Omega, \\ F_t(\mathbf{x}) &= 1, & \mathbf{x} \in \Gamma_2, \end{aligned} \quad (66)$$

and

$$\begin{aligned} -\nabla F_r(\mathbf{x}) \cdot \nabla T_r(\mathbf{x}) &= 0, & \mathbf{x} \in \Omega_1, \\ F_r(\mathbf{x}) &= 1, & \mathbf{x} \in \Gamma_1. \end{aligned} \quad (67)$$

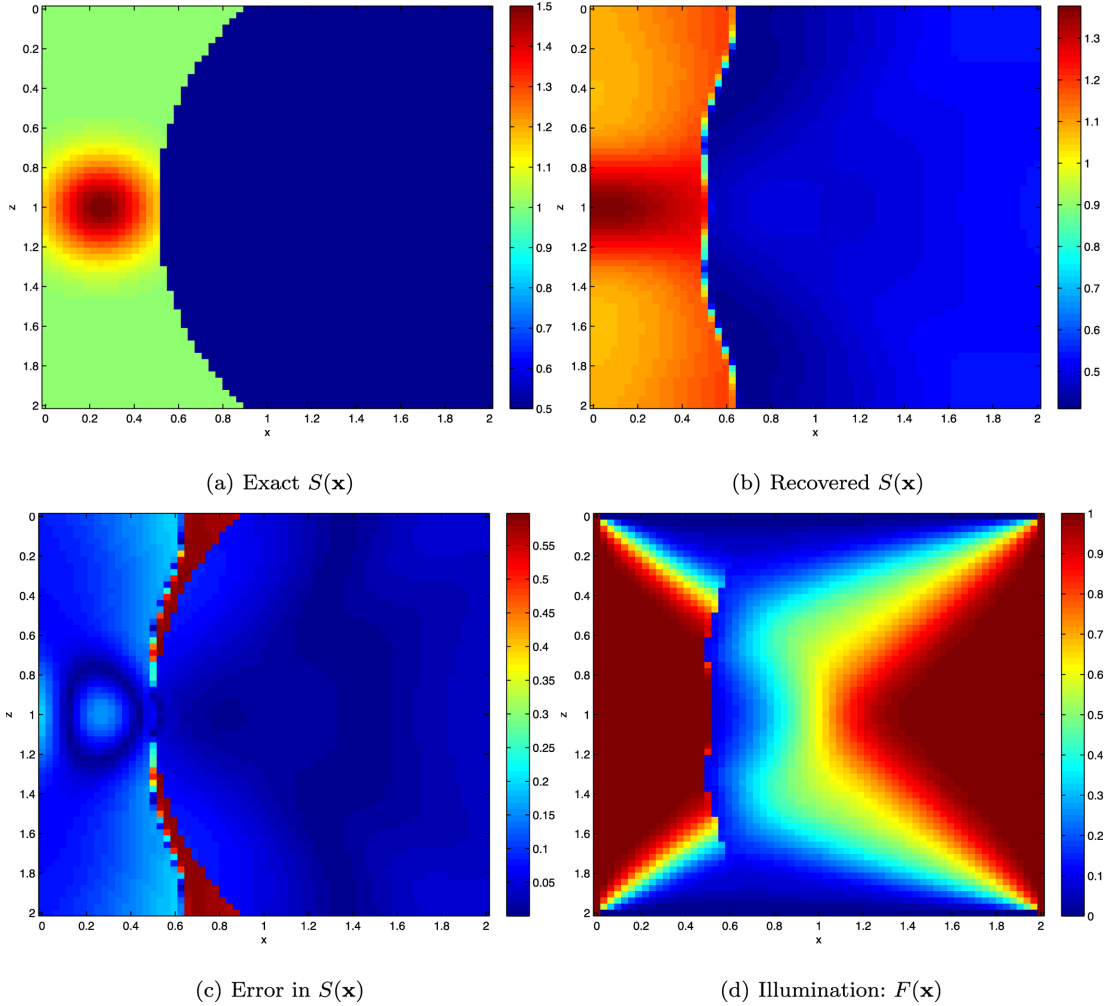


Figure 5. (Example 1, Case 2): piecewise continuous structure, results after 10 000 iterations.

The overall labelling function used to indicate the illuminated region in Ω is defined as

$$F(\mathbf{x}) = \max \{F_t(\mathbf{x}), F_r(\mathbf{x})\}. \quad (68)$$

Another interpretation of this labelling function $F(\mathbf{x})$ is given as follows. $F(\mathbf{x}) = 1$ means that there exists a first-arrival ray connecting one of the receivers, the point source and also the location \mathbf{x} , while $F(\mathbf{x}) = 0$ implies that either there is no ray passing through \mathbf{x} or the passing ray does not reach any receiver. Since this labelling function $F(\mathbf{x})$ highlights all locations where we can find a first-arrival ray joining the given point source to any one of receivers, in fact it leads to ray path coverage. In a typical Lagrangian formulation, one has to shoot various rays to determine this coverage. In the current proposed Eulerian framework, on the other hand, such ray path coverage can be obtained by solving the above advection equations.

The above derivation is for one data set corresponding to a single point source \mathbf{x}_s . If we have multiple point sources $\{\mathbf{x}_s^j, j = 1, 2, \dots, N\}$ corresponding to multiple shots, then the labelling function $F(\mathbf{x})$ is defined as

$$F(\mathbf{x}) = \frac{1}{N} \sum_{j=1}^N F_j(\mathbf{x}), \quad (69)$$

where each $F_j(\mathbf{x})$ is generated by eqs (66)–(68) using the transmission traveltime $T_t^j(\mathbf{x})$ and the reflection traveltime $T_r^j(\mathbf{x})$ corresponding to the j th point source \mathbf{x}_s^j . We can expect that in the region with a larger $F(\mathbf{x})$ (closer to 1) the reconstructed slowness $S(\mathbf{x})$ is more reliable.

5 NUMERICAL IMPLEMENTATION

In this section, we summarize the above algorithm and discuss the numerical implementation in details.

5.1 Algorithm for slowness reconstruction

- Step 1. Initialize ϕ^k, S_1^k and S_2^k for $k = 0$.
- Step 2. Construct $S(\mathbf{x})$ using (7).
- Step 3. Obtain $T_{t,j}(\mathbf{x})$ and $T_{r,j}(\mathbf{x})$ by solving (1)–(2) and (3)–(4) for each point source $\mathbf{x}_s^j, j = 1, 2, 3, \dots, N$.
- Step 4. Obtain $\lambda_j(\mathbf{x}), \mu_j(\mathbf{x})$ and $\hat{\mu}_j(\mathbf{x})$ by solving the adjoint state eqs (54)–(56), respectively, for $j = 1, 2, 3, \dots, N$.
- Step 5. Compute $\tilde{\phi}^k, \tilde{S}_1^k$ and \tilde{S}_2^k using formulas (59), (60) and (61), respectively.
- Step 6. Update $\phi^{k+1} = \phi^k + \epsilon \cdot \nu \tilde{\phi}^k, S_1^{k+1} = S_1^k + \epsilon \cdot \tilde{S}_1^k,$ and $S_2^{k+1} = S_2^k + \epsilon \cdot \tilde{S}_2^k$.

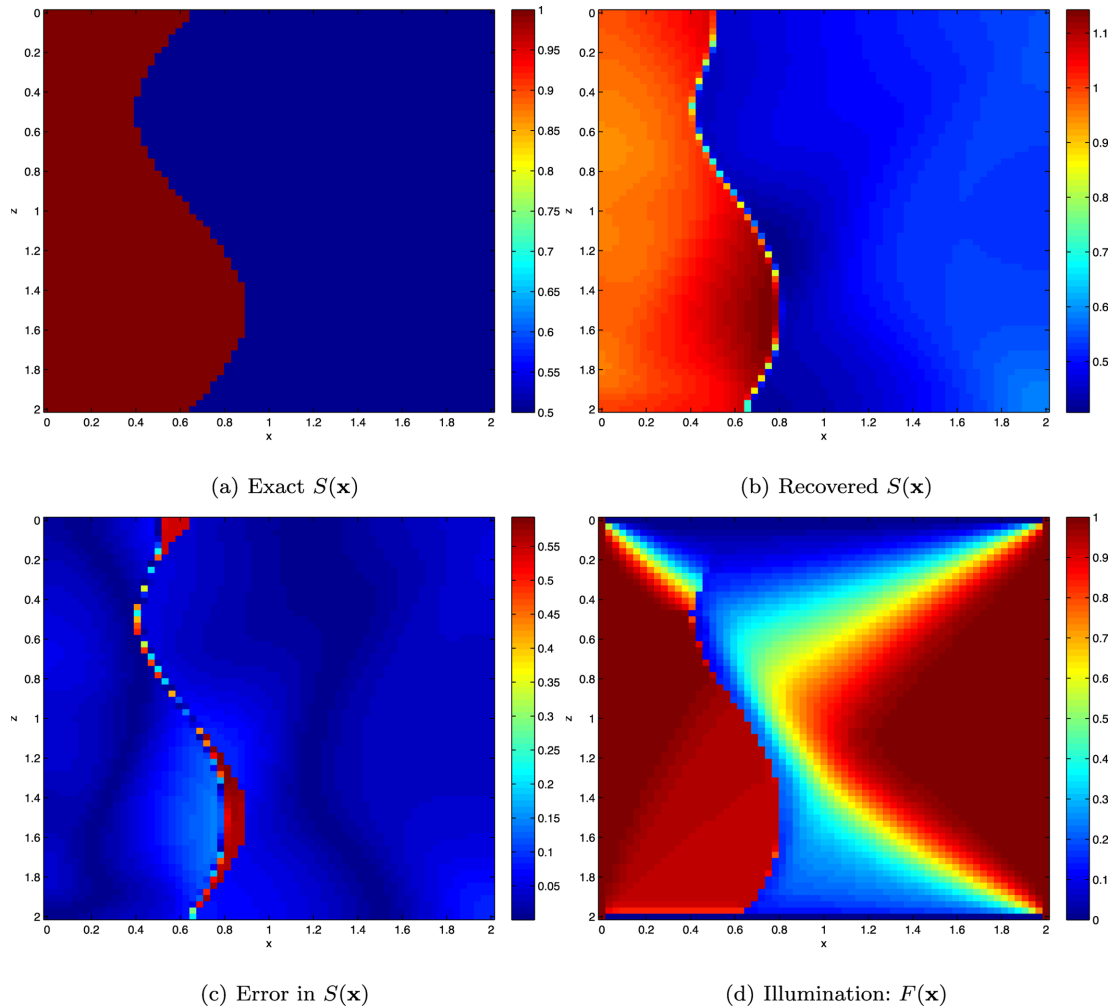


Figure 6. (Example 2, Case 1): piecewise homogeneous structure.

- Step 7. Re-initialize ϕ^{k+1} by solving (39–41), and use Φ to update ϕ^{k+1} .
- Step 8. Go back to step 2 until the mismatch functional $E \leq \delta$ or the iteration step $k \geq k_{\max}$ for some given convergence parameters δ and k_{\max} .

Numerically, the Hamilton–Jacobi equation in step 3 can be efficiently solved using the fast sweeping methods (Tsai *et al.* 2003; Kao *et al.* 2004, 2005; Zhao 2005; Qian *et al.* 2007a,b; Kao *et al.* 2008; Luo *et al.* 2012, 2014). In this work, we follow (Zhao 2005) and have implemented the local solver based on the Godunov Hamiltonian. For the reflection traveltime T_r the system of (3)–(4) is defined in $\Omega_1 \subset \Omega$, which is usually a non-square domain. To maintain a finite difference discretization we solve T_r in the whole domain Ω and impose the boundary condition using the level-set function $\phi(\mathbf{x})$. Specifically, since $\phi(\mathbf{x})$ is maintained to be the signed distance to R , we have $\phi(\mathbf{x}) < 0$ in Ω_1 while $\phi(\mathbf{x}) > 0$ in Ω_2 ; consequently, the boundary condition (4) is implemented by setting

$$T_r(\mathbf{x}) = T_i(\mathbf{x}), \quad \mathbf{x} \in \{\mathbf{x} : \phi(\mathbf{x}) \geq 0\} \tag{70}$$

so that we solve (3) in the whole domain Ω and update $T_r(\mathbf{x})$ only when $\phi(\mathbf{x}) < 0$.

In step 4, we solve the adjoint state eqs (54)–(56) by a fast-sweeping type method as detailed in Leung & Qian (2006). Here we mention the treatment of the boundary conditions for (55) and

(56), which aims to maintain the finite-difference discretization in the non-square domain Ω_1 . Firstly, the non-structured part of $\partial\Omega_1$ is due to the reflector R . Mathematically the reflector R is expressed by $R = \phi^{-1}(0)$. Numerically, however, we may have no exactly zero-valued $\phi(\mathbf{x})$ at any gridpoint. To be consistent with the boundary treatment (70) for the solution of $T_r(\mathbf{x})$, we locate the numerical reflector R using the following strategy: a gridpoint $\mathbf{x}_{i,j}$ is labelled to be the numerical reflector if

$$0 \leq \phi(\mathbf{x}_{i,j}) < \delta \quad (\delta = 3\Delta x \text{ in our implementation})$$

and

$$\left\{ \begin{aligned} &\phi(\mathbf{x}_{i-1,j}) < 0, \text{ or } \phi(\mathbf{x}_{i+1,j}) < 0, \\ &\text{or } \phi(\mathbf{x}_{i,j-1}) < 0, \text{ or } \phi(\mathbf{x}_{i,j+1}) < 0 \end{aligned} \right\}.$$

Then we solve (55) and (56) in the whole domain Ω . For (55), we extend the coefficient $\nabla T_{r,j}$ to the whole domain Ω by setting

$$\nabla T_{r,j} = \begin{cases} \nabla T_{r,j}, & \mathbf{x} \in \Omega_1 \cup R, \\ 0, & \mathbf{x} \in \Omega \setminus (\Omega_1 \cup R), \end{cases}$$

where $\Omega_1 = \{\mathbf{x} : \phi(\mathbf{x}) < 0\}$ and R is the numerical reflector indicated as above. The fast sweeping iteration is performed in the whole Ω with the initial guess $\mu_j = 0$ everywhere. One finds that in the

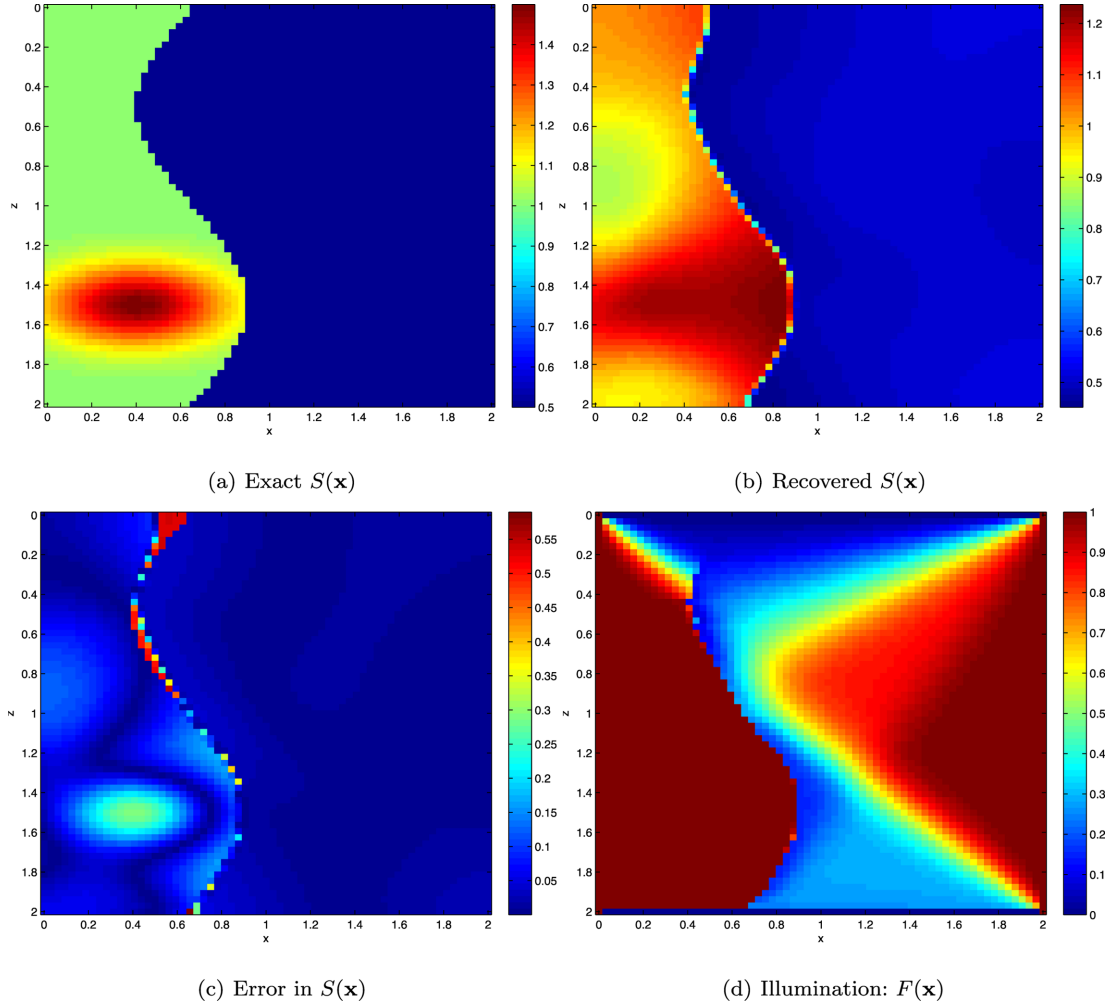


Figure 7. (Example 2, Case 2): piecewise continuous structure.

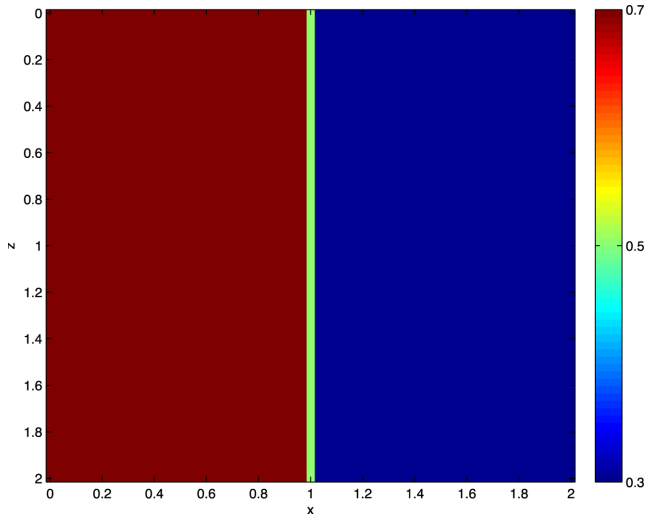


Figure 8. (Example 3): initial guess of $S(\mathbf{x})$.

region $\nabla T_{r,j} = 0$, μ_j is not updated. Thus we actually compute μ_j in $\Omega_1 \cup R$ and extend the value to Ω automatically with $\mu_j = 0$ in $\Omega \setminus (\Omega_1 \cup R)$. The value of $\mu_j|_R$ is needed for the boundary condition on R in (56).

For (56), the coefficient $\nabla T_{t,j}$ is set to be

$$\nabla T_{t,j} = \begin{cases} \nabla T_{t,j}, & \mathbf{x} \in \Omega_1, \\ 0, & \mathbf{x} \in \Omega \setminus \Omega_1, \end{cases}$$

and the fast sweeping iteration is performed in Ω with the initial guess $\hat{\mu}_j = 0$ everywhere. Again one finds that we only update $\hat{\mu}_j$ in Ω_1 and extend the value to the whole domain Ω automatically with $\hat{\mu}_j = 0$ in $\Omega \setminus \Omega_1$. We mention that the gradient of the traveltime is calculated using the third-order WENO scheme (Liu *et al.* 1994) in the inner grids while using the first-order upwind scheme near the boundary.

Finally, we provide a local level set implementation in updating $\phi(\mathbf{x})$, which reduces the overall computational complexity. Based on (7) for the slowness distribution, the level set function $\phi(\mathbf{x})$ mainly contributes near the reflector $R = \phi^{-1}(0)$. Thus we can update the value of ϕ only in a small tube containing R , and the re-initialization strategy maintains ϕ the signed distance function. Specifically, in step 5 and step 6 we evaluate $\tilde{\phi}^k$ and update ϕ^{k+1} only in the computational tube $\{\mathbf{x}: |\phi(\mathbf{x})| < \epsilon_{\text{local}}\}$, where ϵ_{local} is a parameter controlling the width of the tube. This strategy helps to speed up the overall algorithm since we do not need to determine $\tilde{\phi}(\mathbf{x})$ and $\phi^{\text{new}}(\mathbf{x})$ for all gridpoints in the whole computational domain.

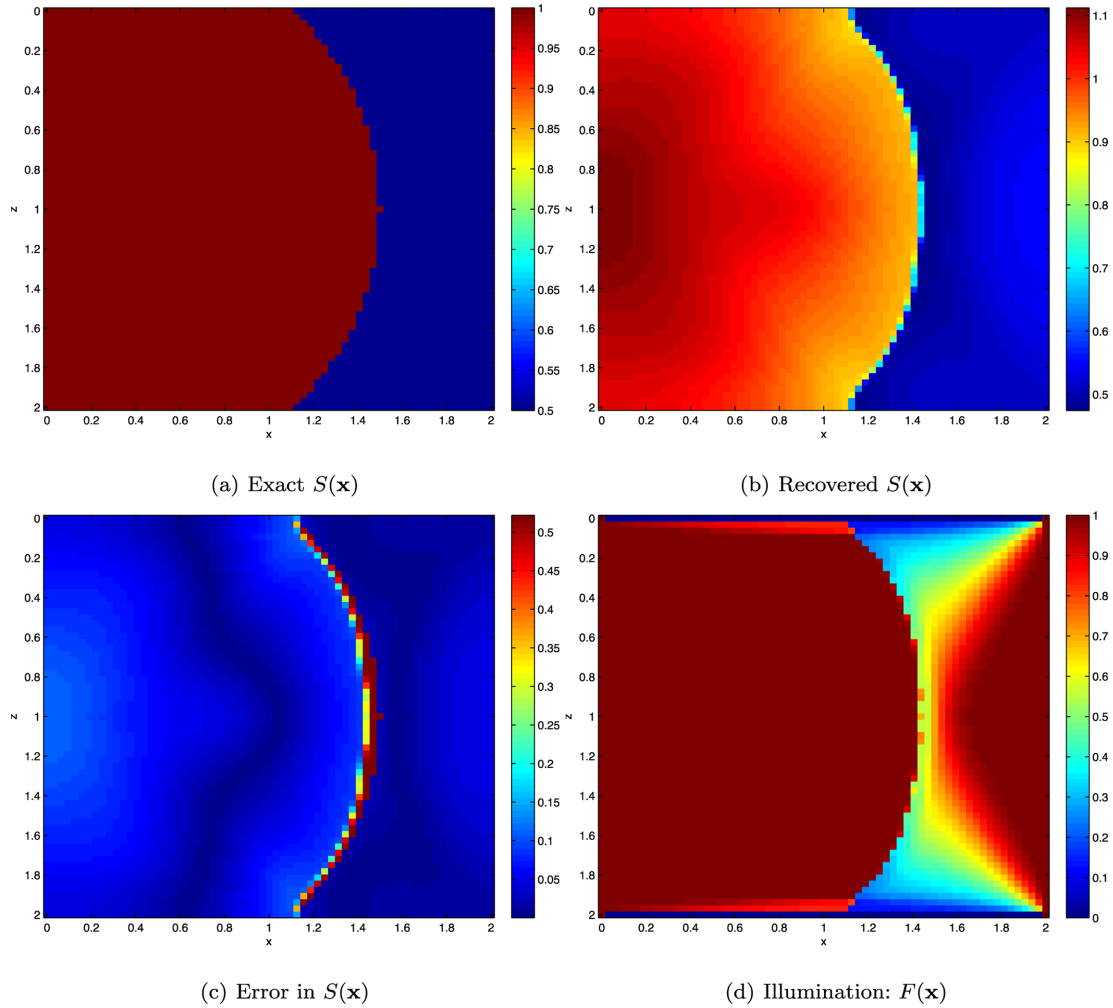


Figure 9. (Example 3, Case 1): piecewise homogeneous structure.

5.2 Algorithm for identifying the illuminated region

- Step 1. Apply the reconstructed slowness $S(\mathbf{x})$ into (1)–(2) and eqs (3)–(4) to solve $T_{t,j}(\mathbf{x})$ and $T_{r,j}(\mathbf{x})$ for each point source $\mathbf{x}_j^j, j = 1, 2, 3, \dots, N$.
- Step 2. For $j = 1, 2, 3, \dots, N$, obtain $F_{t,j}(\mathbf{x})$ and $F_{r,j}(\mathbf{x})$ by solving (66) and (67), and then generate $F_j(\mathbf{x}) = \max\{F_{t,j}(\mathbf{x}), F_{r,j}(\mathbf{x})\}$.
- Step 3. Obtain $F(\mathbf{x}) = \frac{1}{N} \sum_{j=1}^N F_j(\mathbf{x})$.

In step 2, we also use the fast sweeping method developed in Leung & Qian (2006), Li & Leung (2013) to solve the advection equation. Briefly, to solve the advection equation

$$a \cdot \frac{\partial F}{\partial x} + b \cdot \frac{\partial F}{\partial y} = 0,$$

we use the following scheme:

$$\left[a_{i,j}^+ \cdot \frac{F_{i,j} - F_{i-1,j}}{\Delta x} + a_{i,j}^- \cdot \frac{F_{i+1,j} - F_{i,j}}{\Delta x} \right] + \left[b_{i,j}^+ \cdot \frac{F_{i,j} - F_{i,j-1}}{\Delta y} + b_{i,j}^- \cdot \frac{F_{i,j+1} - F_{i,j}}{\Delta y} \right] = 0, \quad (71)$$

where we denote $a^+ = \max\{a, 0\}$ and $a^- = \min\{a, 0\}$. (71) implies that

$$\left(\frac{a_{i,j}^+ - a_{i,j}^-}{\Delta x} + \frac{b_{i,j}^+ - b_{i,j}^-}{\Delta y} \right) \cdot F_{i,j} = \frac{a_{i,j}^+ \cdot F_{i-1,j} - a_{i,j}^- \cdot F_{i+1,j}}{\Delta x} + \frac{b_{i,j}^+ \cdot F_{i,j-1} - b_{i,j}^- \cdot F_{i,j+1}}{\Delta y},$$

and this gives an expression to build up a fast sweeping-type iterative method. Note that to guarantee $F(\mathbf{x}) = 0$ in the unilluminated region, we initialize $F(\mathbf{x}) = 0$ everywhere. We update $F_{i,j}$ only in the interior region of Ω and set $F_{i,j} = 0$ on the boundary where no receivers are located. This is because eikonal solvers based on the fast sweeping approach usually generate artificial creeping rays along the boundary (Fomel *et al.* 2009) and we do not want such artificial ray polluting the computation of our labelling function.

Furthermore, the advection system (67) is defined in $\Omega_1 \subset \Omega$ which is usually non-rectangular. To maintain a regular finite-difference discretization, we extend (67) to the whole domain Ω by setting

$$\nabla T_r(\mathbf{x}) = \begin{cases} \nabla T_r(\mathbf{x}), & \mathbf{x} \in \Omega_1, \\ 0, & \mathbf{x} \in \Omega \setminus \Omega_1, \end{cases}$$

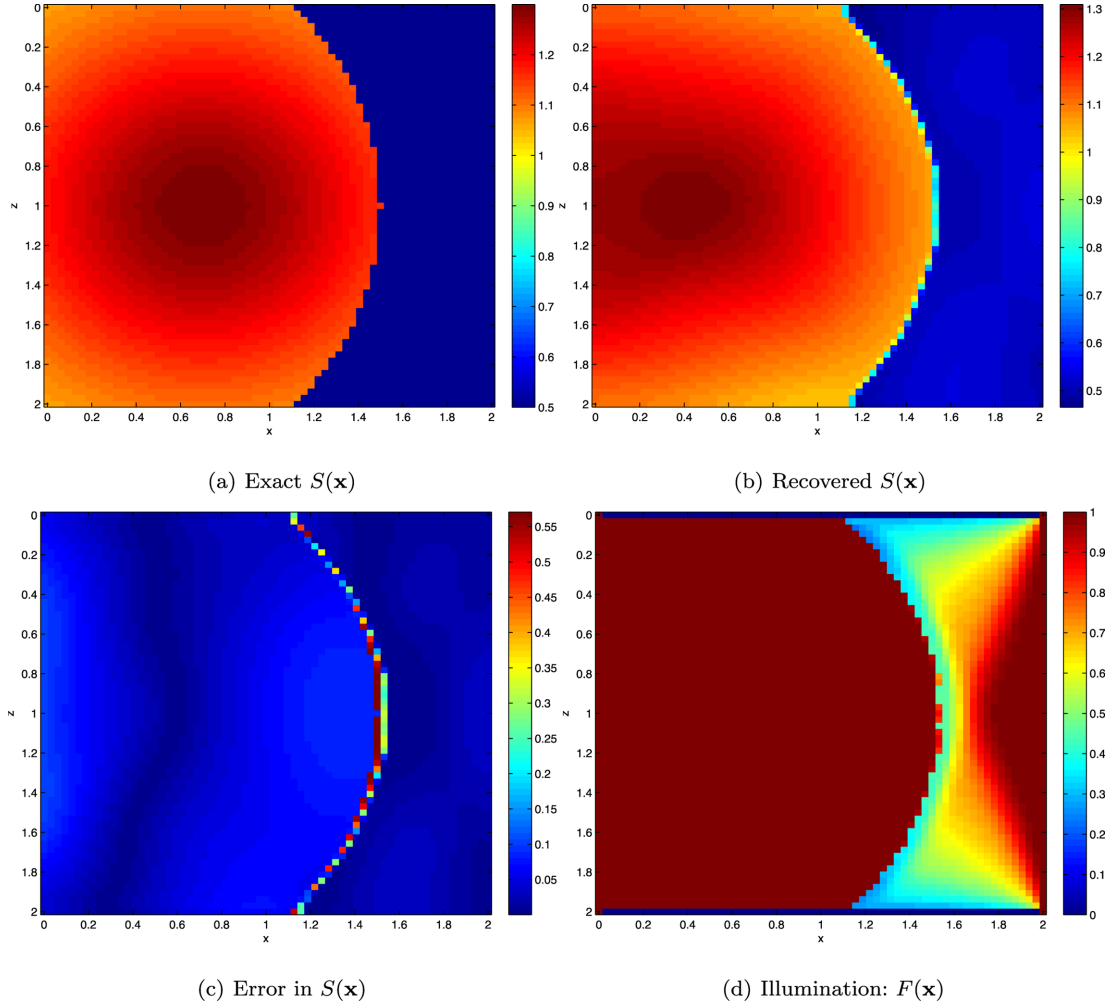


Figure 10. (Example 3, Case 2): piecewise continuous structure.

where $\Omega_1 = \{\mathbf{x}: \phi(\mathbf{x}) < 0\}$, $\Omega \setminus \Omega_1 = \{\mathbf{x}: \phi(\mathbf{x}) \geq 0\}$ and $\phi(\mathbf{x})$ is the level set function in the reconstructed $S(\mathbf{x})$. Then we perform the fast sweeping iteration for (67) in Ω , but $F_r(\mathbf{x})$ is updated only in $\Omega_1 = \{\mathbf{x}: \phi(\mathbf{x}) < 0\}$.

6 NUMERICAL EXPERIMENTS

In all examples, the smoothing parameter τ in the numerical Heaviside function $H_\tau(\mathbf{x})$ is chosen to be $\tau = 0.01$, and the updating step size is fixed to be $\epsilon = 10^{-3}$. The parameter to reduce the perturbation of ϕ is $\nu = 0.1$, the weight of the regularization term in ϕ is $\gamma = 0.01$, and the weight in controlling the amount of regularity in \hat{S}_1 and \hat{S}_2 is $\alpha = 1$. Furthermore, the width of the computational tube for the local level-set implementation is set to be $\epsilon_{\text{local}} = 4\Delta x$.

6.1 2-D examples

The computational domain is set to be $\Omega = [0, 2] \times [0, 2]$ which is discretized using 65×65 mesh grids. We assume that $N = 49$ point sources are located along one side of the domain: $(x_s^j, z_s^j) = (0.05, 0.04j)$, $j = 1, 2, \dots, N$. In all these examples, we have receivers on all the grid nodes along $\Gamma_2 = \{x = 2\}$ to record the

transmission traveltime T_t , and we put receivers on all the grid nodes along $\Gamma_1 = \{x = 0\}$ to record the reflection traveltime T_r .

6.1.1 Example 1: a concave circular reflector

In this example the reflector is defined by $\{(x, z) : x = x(z) = 2 - \sqrt{1.5^2 - (z - 1)^2}, 0 \leq z \leq 2\}$ and the slowness distribution is

$$S(x, z) = \begin{cases} S_1(x, z), & x \leq 2 - \sqrt{1.5^2 - (z - 1)^2}, \\ S_2(x, z), & x > 2 - \sqrt{1.5^2 - (z - 1)^2}. \end{cases}$$

Case 1: a piecewise homogeneous model with $S_1(x, z) = 1$ and $S_2(x, z) = 0.5$. We start the iteration with initial guess $S_1^0 = 1.5$, $S_2^0 = 0.3$ and $\phi^0(\mathbf{x}) = x - 1$. The initial slowness function $S(\mathbf{x})$ is shown in Fig. 2. Fig. 3 provides the numerical results after 10 000 iterations. One finds that the structure is well recovered and the error mainly appears in the region near the discontinuity. Also the illumination is clearly identified by our labelling function $F(\mathbf{x})$ in (d). We can see that for those regions where the function $F(\mathbf{x})$ is close to one, the inversion result is very accurate. Near the boundary of the computational domain (for example, near $x = 0.6$ and z near 0 and 2), on the other hand, $F(\mathbf{x})$ is close to zero; this implies that there are few rays passing through those regions in terms of

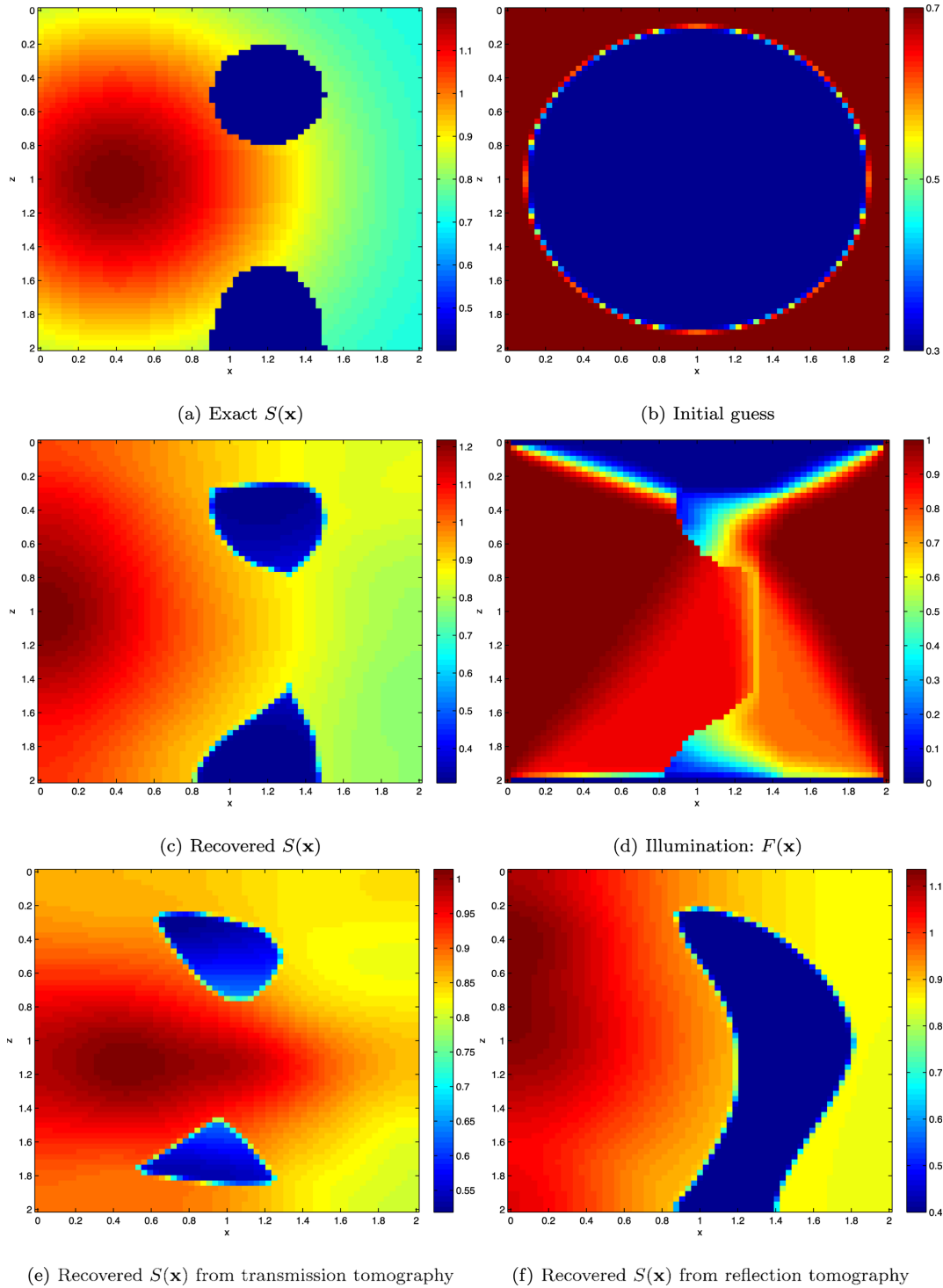


Figure 11. (Example 4, Case 1): disconnecting reflector.

first-arrival rays between all source–receiver pairs, and this explains why the reconstruction in those regions incurs relatively large errors.

We emphasize again that our labelling function $F(\mathbf{x})$ indeed gives a simple representation of ray path coverage in the first-arrival sense in the Eulerian framework. To compare our illumination function $F(\mathbf{x})$ with the ray path coverage, we have also extracted several Lagrangian ray paths in Fig. 4. In particular, we have shown some rays emitted from the point sources at $(x_s, z_s) = (0.05, 0.08)$ in Figs 4(a) and (b) and $(x_s, z_s) = (0.05, 1)$ in Figs 4(c) and (d), respectively.

Case 2: a piecewise continuous model with

$$S_1(x, z) = 1 + 0.5 \cdot \exp\{-16[(x - 0.25)^2 + (z - 1)^2]\}$$

and $S_2(x, z) = 0.5$. The initial guess of $S(\mathbf{x})$ is the same as shown in Fig. 2. We perform 10 000 iterations, and Fig. 5 shows the numerical results. One finds that the shape of the reflector is well recovered and the slowness distribution including the anomaly structure is well recovered.

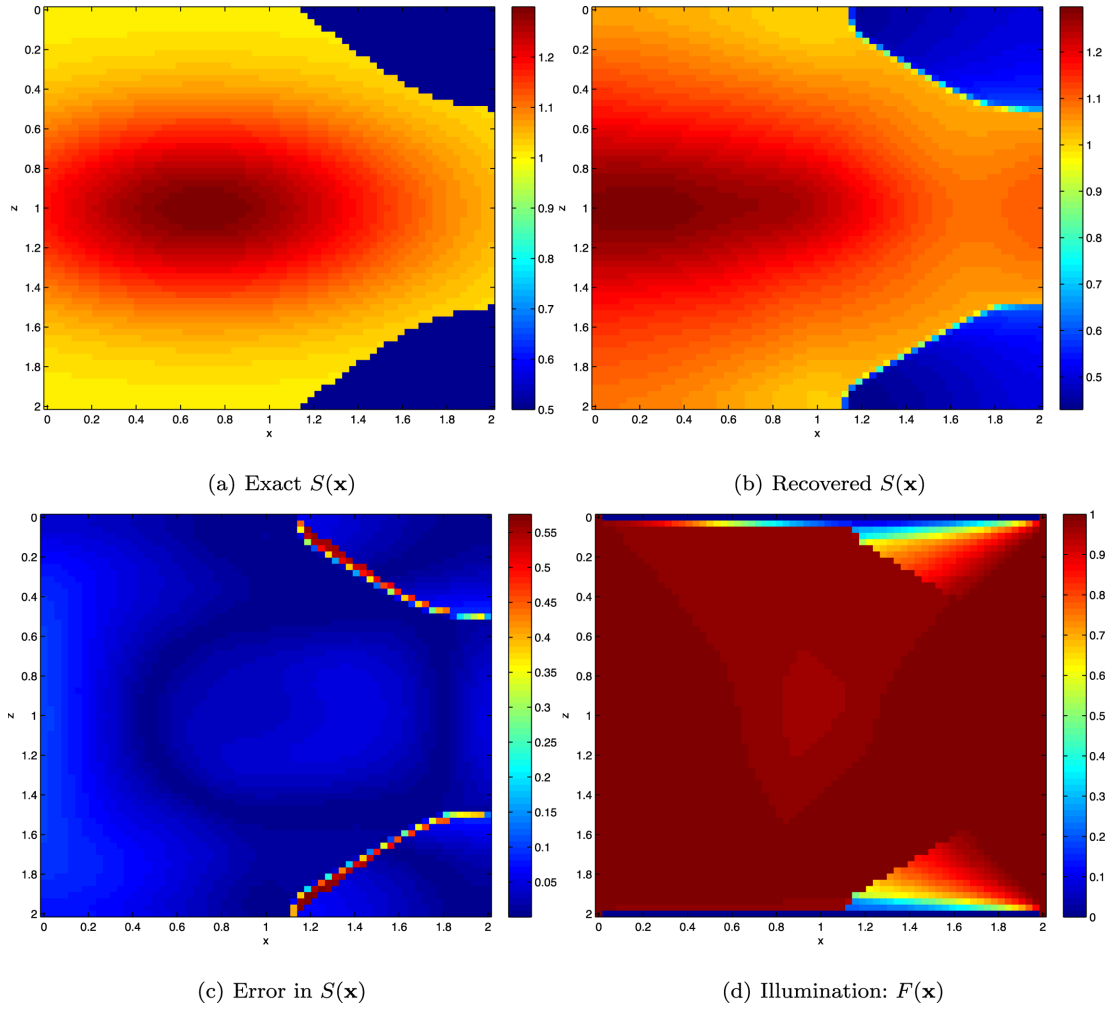


Figure 12. (Example 4, Case 2: no noise): disconnecting reflector.

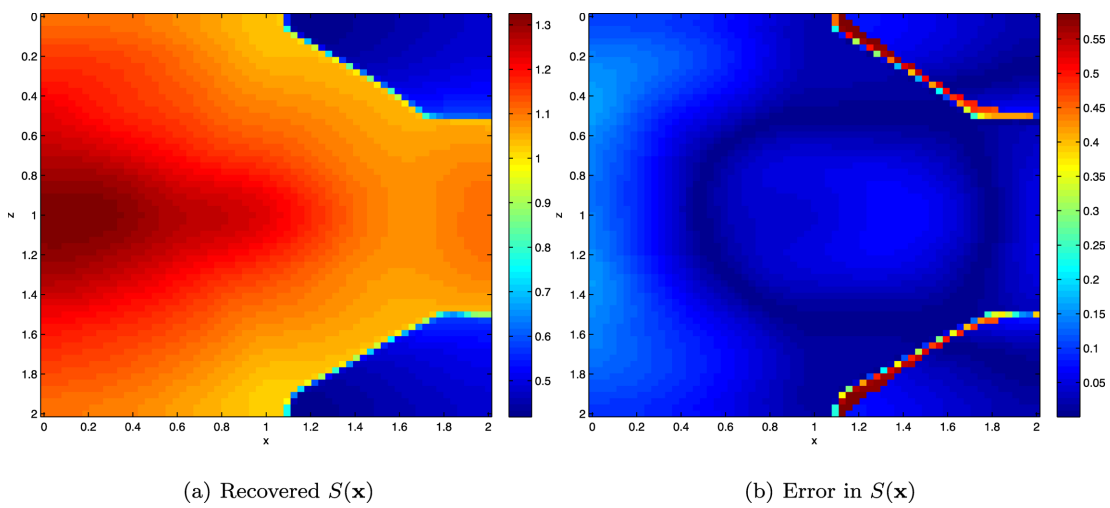


Figure 13. (Example 4, Case 2: with noise) 2 per cent Gaussian noise with zero mean is added to the clean measurements in Fig. 12.

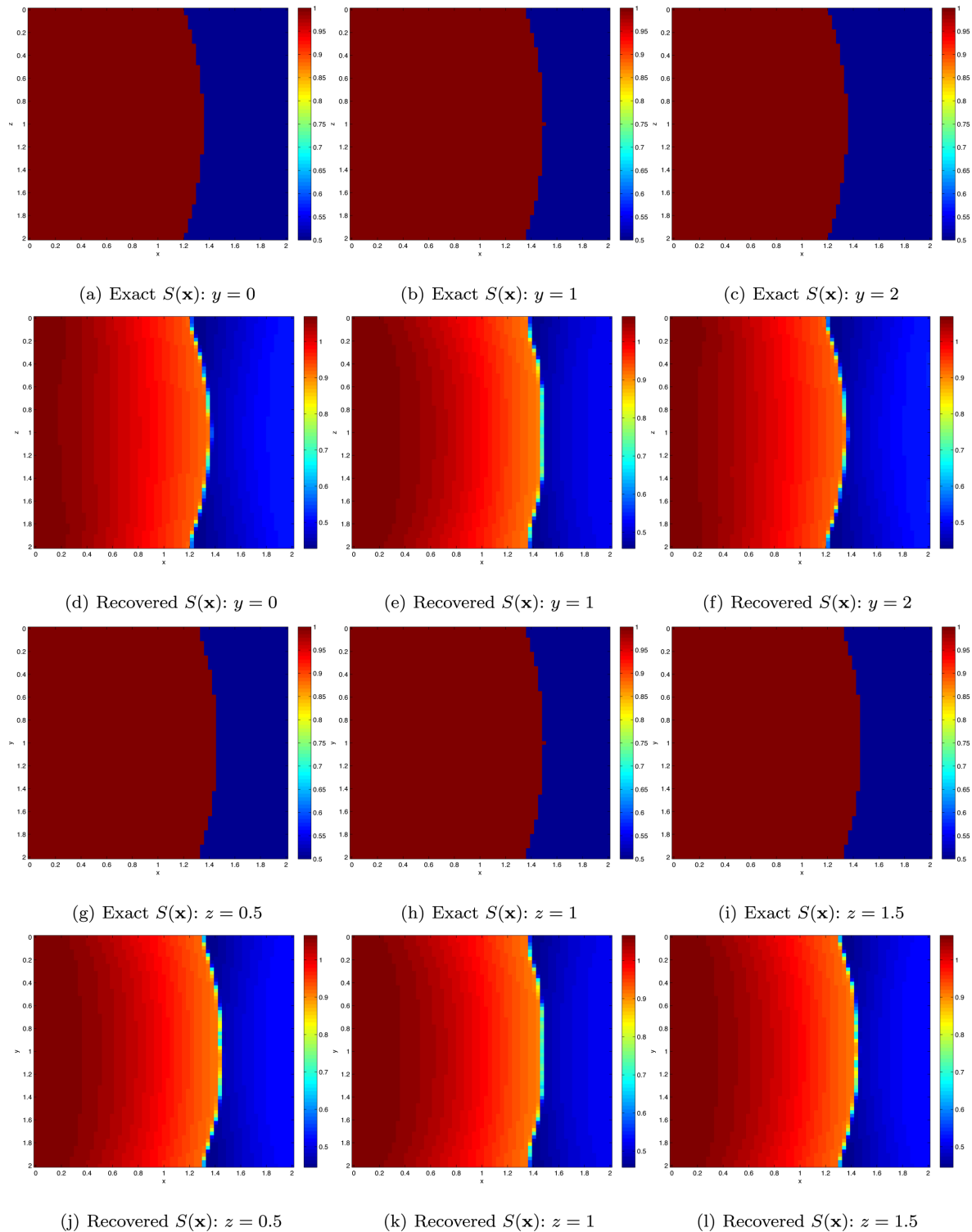


Figure 14. (Example 5, Case 1): 3-D tomography, piecewise homogeneous structure. Panels (a)–(c) and (g)–(i): exact slowness with slices $y = 0, 1, 2$ and $z = 0.5, 1, 1.5$. Panels (d)–(f) and (j)–(l): results after 2000 iterations with slices $y = 0, 1, 2$ and $z = 0.5, 1, 1.5$.

6.1.2 Example 2: a sinusoidal reflector

The sinusoidal reflector is defined by $\{(x, z): x = x(z) = 0.65 - 0.25 \sin(\pi z), 0 \leq z \leq 2\}$ and the slowness distribution is

$$S(x, z) = \begin{cases} S_1(x, z), & x \leq 0.65 - 0.25 \sin(\pi z), \\ S_2(x, z), & x > 0.65 - 0.25 \sin(\pi z). \end{cases}$$

We have tested two cases with the initial guess for $S(\mathbf{x})$ as shown in Fig. 2.

Case 1: a piecewise homogeneous model with $S_1(x, z) = 1$ and $S_2(x, z) = 0.5$. We perform 20 000 iterations and the final numerical results are shown in Fig. 6. We get a perfect reconstruction for the shape of the reflector. In the recovered $S(\mathbf{x})$ as shown in (b), the

rough structure is correct and the error is acceptable, though there are shadow regions which deviate from the homogeneity.

Case 2: a piecewise continuous model with

$$S_1(x, z) = 1 + 0.5 \cdot \exp \left\{ - \left[\frac{(x - 0.4)^2}{0.4^2} + \frac{(z - 1.5)^2}{0.2^2} \right] \right\}$$

and $S_2(x, z) = 0.5$. We perform 11 000 iterations and the numerical results are shown in Fig. 7. The shape of the reflector is well recovered. The recovered anomaly in $S(\mathbf{x})$ is not perfect due to the inherent heterogeneity. However, the reconstruction in (b) still provides us with useful information in understanding the structure.

In both cases, we found that the large errors in the construction occur near the region where the illumination is low, that is when $F(\mathbf{x})$ is relatively small. For example, in region near $x = 0.6$ and $z = 0$, there are just a few first-arrival rays joining any source–receiver pairs. It is, therefore, extremely challenging to recover the velocity model in those regions.

6.1.3 Example 3: a convex circular reflector

In this example, the reflector is now moved further away from the sources and is defined by

$$\{(x, z) : x = x(z) = \sqrt{1.5^2 - (z - 1)^2}, \quad 0 \leq z \leq 2\}.$$

The slowness distribution is

$$S(x, z) = \begin{cases} S_1(x, z), & x \leq \sqrt{1.5^2 - (z - 1)^2}, \\ S_2(x, z), & x > \sqrt{1.5^2 - (z - 1)^2}. \end{cases}$$

Case 1: a piecewise homogeneous model with $S_1(x, z) = 1$ and $S_2(x, z) = 0.5$. We start the iteration with the initial guess $S_1^0 = 0.7$, $S_2^0 = 0.3$ and $\phi^0(\mathbf{x}) = x - 1$. The initial slowness function $S(\mathbf{x})$ is shown in Fig. 8. Fig. 9 shows the numerical results after 10 000 iterations. Both the piecewise structure and the reflector are well recovered.

Case 2: a piecewise continuous model with $S_1(x, z) = 1 + 0.3 \cdot \exp \{ -[(x - 0.7)^2 + (z - 1)^2] \}$ and $S_2(x, z) = 0.5$. The initial guess of $S(\mathbf{x})$ is the same as shown in Fig. 8. Fig. 10 shows the numerical results after 13 000 iterations. From the plot of error in Fig. 10(c), one finds that the location of the reflector is perfectly recovered. Also we get a good inversion of the slowness distribution including the non-homogeneous structure beyond the reflector.

6.1.4 Example 4: irregular reflectors

In this example, we consider more challenging cases where the true reflector has an irregular shape. We will demonstrate that starting from a regular initial guess of the true reflector in terms of an initial level-set function, the level-set defined interface will undergo topological changes during the level-set evolution in the energy minimization process, and the level-set method can handle such topological changes naturally.

Case 1: the exact reflectors are given by the two disjoint curves $\frac{(x-1.2)^2}{0.3^2} + \frac{(z-2)^2}{0.5^2} = 1$ and $(x - 1.2)^2 + (z - 0.5)^2 = 0.3^2$. The slowness distribution is

$$S(x, z) = \begin{cases} S_2(x, z), & \frac{(x-1.2)^2}{0.3^2} + \frac{(z-2)^2}{0.5^2} \leq 1, \\ S_2(x, z), & (x - 1.2)^2 + (z - 0.5)^2 \leq 0.3^2, \\ S_1(x, z), & \text{otherwise,} \end{cases}$$

where $S_1(x, z) = 0.7 + 0.5 \cdot \exp \{ -[(x - 0.4)^2 + (z - 1)^2] \}$ and $S_2(x, z) = 0.4$. This exact solution is shown in Fig. 11(a). The initial

guess for $S(\mathbf{x})$ is shown in Fig. 11(b), where $S_1^0 = 0.7$, $S_2^0 = 0.3$ and $\phi^0(\mathbf{x}) = 0.9 - \sqrt{(x - 1)^2 + (z - 1)^2}$. Fig. 11(c) plots the solution after 3000 iterations. Our proposed algorithm can successfully recover the disconnecting reflectors starting from an initial guess where the corresponding reflector has a different shape. This example demonstrates that the level set method provides a flexible tool for automatically capturing the correct topology of the interface. Once again, the error in the reconstruction occurs mostly at locations where the illumination is low, that is $F(\mathbf{x})$ is close to zero, as shown in Fig. 11(d).

To demonstrate the improvement in the solution by the joint transmission-reflection tomography, we further provide the recovered slowness using only transmission tomography and reflection tomography in Figs 11(e) and (f), respectively, after 3000 and 1500 iterations. Note that in the reflection tomography, we do not update $S_2(x, z)$ at all because the region inside the reflector is always unilluminated. Comparing solutions from (c), (e) and (f), we found that our joint tomography gives a much better reconstruction solution than using information from only either transmission traveltimes or reflection traveltimes. In particular, we better resolve the structure in the background region comparing to the solution from the transmission tomography, while we also determine the topologically correct solution comparing to the solution from the reflection tomography. Because of the extra information introduced in the minimization formulation, the joint traveltimes tomography indeed gives a more accurate solution for this highly ill-conditioned inverse problem.

Case 2: the reflector is defined by $\{(x, z) : (z - 1)^2 - (x - 2)^2 = 0.25, 0 \leq x \leq 2, 0 \leq z \leq 2\}$, and we consider the slowness distribution given by

$$S(x, z) = \begin{cases} S_1(x, z), & (z - 1)^2 - (x - 2)^2 < 0.25, \\ S_2(x, z), & (z - 1)^2 - (x - 2)^2 \geq 0.25, \end{cases}$$

where $S_1(x, z) = 1 + 0.3 \cdot \exp \{ -[(x - 0.7)^2 + (z - 1)^2/0.25] \}$ and $S_2(x, z) = 0.5$. The initial guess for $S(\mathbf{x})$ is the same as shown in Fig. 8. Fig. 12 provides the numerical results after 6000 iterations. The disconnecting reflectors are well recovered and our reconstruction also approximates the inhomogeneous structure well.

To further test the robustness of the algorithm, we have perturbed the measurements T_i^* and T_r^* by 2 per cent Gaussian noise with zero mean. The results after 6000 iterations are shown in Fig. 13. We found that our reconstruction is not too sensitive to the added noise. The solution in Fig. 13(a) is similar to the recovered solution using the clean measurements as shown in Fig. 12(b).

6.2 A 3-D example

We consider a 3-D example where the domain $\Omega = [0, 2] \times [0, 2] \times [0, 2]$ is discretized by a $65 \times 65 \times 65$ mesh. We put $N = 49$ point sources on one side of the domain: $(x_s, y_s^i, z_s^j) = (0.05, 0.1 + 0.3 \cdot (i - 1), 0.1 + 0.3 \cdot (j - 1))$, $i, j = 1, 2, \dots, 7$. In all these examples, we have receivers at all the grid nodes along $\Gamma_2 = \{x = 2\}$ to record the first-arrival transmission traveltimes T_t , and we put receivers at all the grid nodes along $\Gamma_1 = \{x = 0\}$ to record the reflection traveltimes T_r .

6.2.1 Example 5: a spherical reflector

A 3-D reflector is defined by

$$\{(x, y, z) : x = \sqrt{3.5^2 - (y - 1)^2 - (z - 1)^2} - 2, \quad 0 \leq y \leq 2, 0 \leq z \leq 2\}$$

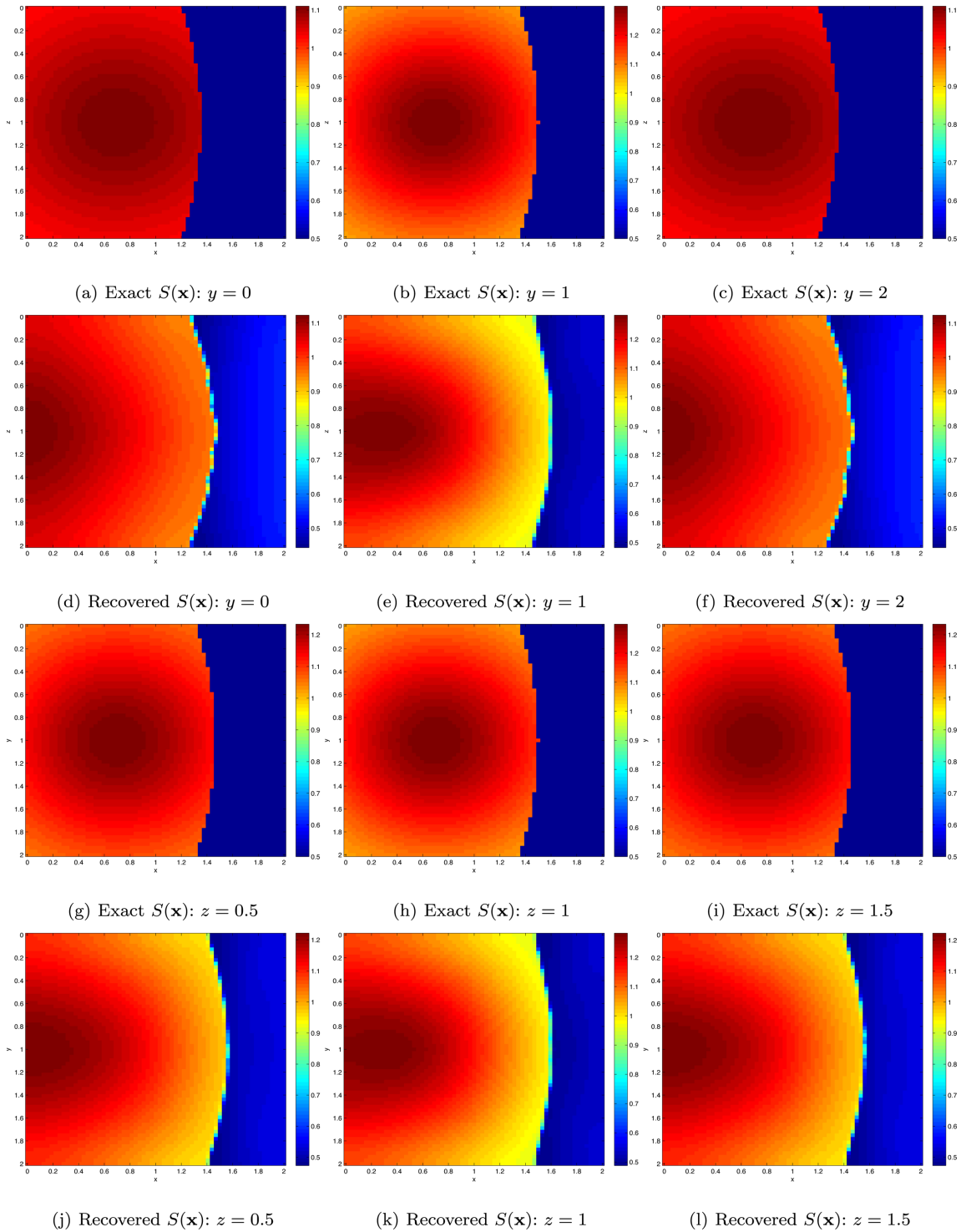


Figure 15. (Example 5, Case 2): 3-D tomography, piecewise continuous structure. Panels (a)–(c) and (g)–(i): exact slowness with slices $y = 0, 1, 2$ and $z = 0.5, 1, 1.5$. Panels (d)–(f) and (j)–(l): Results after 2000 iterations with slices $y = 0, 1, 2$ and $z = 0.5, 1, 1.5$.

and the slowness distribution is

$$S(x, y, z) = \begin{cases} S_1(x, y, z), & x \leq \sqrt{3.5^2 - (y - 1)^2 - (z - 1)^2} - 2, \\ S_2(x, y, z), & x > \sqrt{3.5^2 - (y - 1)^2 - (z - 1)^2} - 2. \end{cases}$$

We have tested two cases, and we start both tests with the same initial guess given by $S_1^0(x, y, z) = 0.7$, $S_2^0(x, y, z) = 0.3$ and $\phi^0(x, y, z) = x - 1$.

Case 1: a piecewise homogeneous model with $S_1(x, y, z) = 1$ and $S_2(x, y, z) = 0.5$. Fig. 14 shows numerical results after 2000 iterations, where the 3-D structure is presented by slices. We plot the slices of $S(\mathbf{x})$ at $y = 0, 1, 2$ and $z = 0.5, 1, 1.5$. The shape of the reflector is perfectly recovered and the deviation in the reconstructed slowness structure is acceptable.

Case 2: a heterogeneous model with $S_1(x, z) = 1 + 0.3 \cdot \exp(-((x - 0.7)^2 + (y - 1)^2 + (z - 1)^2))$ and $S_2(x, z) = 0.5$. Fig. 15 shows

the numerical results after 2000 iterations. Once again, like other 2-D examples, both the shape and the location of the reflector are very well recovered. The inhomogeneous structure in the shallow region is well reconstructed. Even though the exact slowness in the right region is homogeneous, our numerical algorithm does not explicitly impose that constraint but simply looks for a piecewise smooth solution. Our inverted solution approximates well with the exact constant, as shown in Fig. 15.

7 DISCUSSION AND CONCLUSION

In this paper, we have extended the level-set adjoint-state method to solve the joint transmission-reflection tomography problem. We invert for the heterogeneous structure including the location of reflectors using only first-arrival transmission and reflection traveltimes. For the transmission part, the derivation of the adjoint-state method is similar to our previous work in Li & Leung (2013), while the reflection part has to be done differently. The major issue is that we should maintain an inflow boundary condition for the adjoint-state equation such that the information propagates from the receivers on the boundary back into the interior region. We have discussed in details the derivation of two adjoint state equations to handle the reflection part in the mismatch functional. Furthermore, we have also proposed an easily computed quantity which can be used to quantify the reliability of the reconstruction and can also be regarded as an Eulerian interpretation of ray path coverage in the first-arrival sense.

Various synthetic examples have been considered in the paper to test the accuracy and robustness of our algorithm. Because of the level-set formulation, the proposed method can handle topological change of the estimated reflector in the energy minimization process. We can recover a complicated structure starting from an initial guess with little assumption on the reflector. We have also demonstrated that the numerical approach is not sensitive to noise in the measurements.

Indeed, one shortcoming of the proposed approach is in the computational efficiency. This is mostly because we use only straightforward gradient descent method in minimizing the mismatching functional, which therefore required thousands of numerical iterations in obtaining satisfactory solution. As a future work, we will incorporate more efficient numerical optimization methods, such as quasi-Newton type methods, into our formulation so that the whole algorithm can be sped up significantly. While we are improving the overall computational efficiency of the algorithm, we expect that our proposed method will be useful for traveltime tomography in practical seismic surveys.

ACKNOWLEDGEMENTS

WL is supported in part by the Hong Kong PhD Fellowship. SL is supported in part by the Hong Kong RGC under Grant GRF603011. Qian is partially supported by NSF-1115363 and NSF-1222368.

REFERENCES

Aki, K. & Lee, W.H.K., 1976. Determination of the three-dimensional velocity anomalies under a seismic array using first P arrival times from local earthquakes I. A homogeneous initial model, *J. geophys. Res.*, **81**, 4381–4399.

- Aki, K. & Richards, P., 1980. *Quantitative Seismology*, Freeman and Co.
- Ammon, C. & Vidale, J., 1993. Tomography without rays, *Bull. seism. soc. Am.*, **83**, 509–528.
- Berryman, J., 2000a. Analysis of approximate inverses in tomography I. Resolution analysis of common inverses, *Opt. Eng.*, **1**, 87–115.
- Berryman, J., 2000b. Analysis of approximate inverses in tomography II. iterative inverses, *Opt. Eng.*, **1**, 437–473.
- Bishop, T.N. *et al.*, 1985. Tomographic determination of velocity and depth in laterally varying media, *Geophysics*, **50**, 903–923.
- Bois, P., Porte, M., Levergne, M. & Thomas, G., 1972. Well-to-well seismic measurements, *Geophysics*, **37**, 471–480.
- Bregman, N., Langan, R. & Resnick, J., 1989. Crosshole seismic tomography, *Geophysics*, **54**, 200–215.
- Bube, K., Langan, R. & Resnick, J., 1995. Theoretical and numerical issues in the determination of reflector depths in seismic reflection tomography, *J. geophys. Res.*, **100**, 12 449–12 458.
- Chung, E., Qian, J., Uhlmann, G. & Zhao, H., 2011. An adaptive phase space method with application to reflection traveltime tomography, *Inverse Problems*, **27**, 115002.
- Clarke, R.A., Alazard, B., Pelle, L., Sinuquet, D., Lailly, P., Delprat-Jannaud, F. & Jannaud, L., 2001. 3D traveltime reflection tomography with multi-valued arrivals, in *Proceedings of the 71st Ann. Internat. Mtg., Soc. Expl. Geophys.*, Expanded Abstracts, Soc. Expl. Geophys., Tulsa, OK, pp. 1601–1604.
- Delprat-Jannaud, F. & Lailly, P., 1993. Ill-posed and well-posed formulations of the reflection travel time tomography problem, *J. geophys. Res.*, **98**, 6589–6605.
- Delprat-Jannaud, F. & Lailly, P., 1995. Reflection tomography: how to handle multiple arrivals?, *J. geophys. Res.*, **100**, 703–715.
- Farra, V. & Madariaga, R., 1988. Non-linear reflection tomography, *Geophys. J.*, **95**, 135–147.
- Fomel, S., Luo, S. & Zhao, H., 2009. Fast sweeping method for the factored eikonal equation, *J. Comput. Phys.*, **228**, 6440–6455.
- Hobro, J., Singh, S. & Minshull, T., 2003. Three-dimensional tomographic inversion of combined reflection and refraction seismic traveltime data, *Geophys. J. Int.*, **152**, 79–93.
- Huang, G.-J., Bai, C.-Y., Zhu, D.-L. & Greenhalgh, S., 2012. 2d/3d seismic simultaneous inversion for the velocity and interface geometry using multiple classes of arrivals, *Bull. seism. Soc. Am.*, **102**, 790–801.
- Huang, J.-W. & Bellefleur, G., 2012. Joint transmission and reflection traveltime tomography using the fast sweeping method and the adjoint-state technique, *Geophys. J. Int.*, **188**, 570–582.
- Jing, X.-L., Yang, C.-C. & Wang, S.-Q., 2007. An improved seismic reflection tomographic method, *Chin. J. Geophys.*, **50**, 1588–1594.
- Jurado, F., Sinoquet, D. & Ehinger, A., 1996. 3d reflection tomography designed for complex structures, in *Proceedings of the 1996 SEG Annual Meeting*.
- Kao, C., Osher, S. & Qian, J., 2004. Lax-Friedrichs sweeping schemes for static Hamilton-Jacobi equations, *J. Comp. Phys.*, **196**, 367–391.
- Kao, C.Y., Osher, S. & Qian, J., 2008. Legendre transform based fast sweeping methods for static Hamilton-Jacobi equations on triangulated meshes, *J. Comput. Phys.*, **227**, 10 209–10 225.
- Kao, C.Y., Osher, S.J. & Tsai, Y.-H., 2005. Fast sweeping method for static Hamilton-Jacobi equations, *SIAM J. Num. Anal.*, **42**, 2612–2632.
- Kennett, B., Sambridge, M. & Williamson, P., 1988. Subspace methods for large inverse problems with multiple parameter classes, *Geophys. J. Int.*, **94**, 237–247.
- Lelievre, P., Farquharson, C. & Hurich, C., 2011. Inversion of first-arrival seismic traveltimes without rays, implemented on unstructured grids, *Geophys. J. Int.*, **185**, 749–763.
- Leung, S. & Qian, J., 2005. A transmission tomography problem based on multiple arrivals from paraxial liouville equations: Expanded Abstract for the SEG 75th Annual Meeting.
- Leung, S. & Qian, J., 2006. An adjoint state method for 3D transmission traveltime tomography using first arrival, *Commun. Math. Sci.*, **4**, 249–266.

- Leung, S. & Qian, J., 2007. Transmission traveltime tomography based on paraxial liouville equations and level set formulations, *Inverse Problems*, **23**, 799–821.
- Li, W. & Leung, S., 2013. A fast local level set adjoint state method for first arrival transmission traveltime tomography with discontinuous slowness, *Geophys. J. Int.*, **195**(1), 582–596.
- Liu, X.D., Osher, S.J. & Chan, T., 1994. Weighted essentially nonoscillatory schemes, *J. Comput. Phys.*, **115**, 200–212.
- Luo, S., Qian, J. & Burridge, R., 2014. High-order factorization based high-order hybrid fast sweeping methods for point-source eikonal equations, *SIAM J. Numer. Anal.*, **52**, 23–44.
- Luo, S., Qian, J. & Zhao, H.-K., 2012. Higher-order schemes for 3-D traveltimes and amplitudes, *Geophysics*, **77**, T47–T56.
- Lutter, W., Nowack, R. & Braile, L., 1990. Seismic imaging of upper crustal structure using travel times from the PASSCAL Ouachita experiment, *J. geophys. Res.*, **95**, 4621–4631.
- McCaughey, M. & Singh, S., 1997. Simultaneous velocity and interface tomography of normal-incidence and wide-aperture seismic traveltime data, *Geophys. J. Int.*, **131**, 87–99.
- McMechan, G., Harris, J. & Anderson, L., 1987. Crosshole tomography for strongly variable media with applications to scale model data, *Bull. seism. Soc. Am.*, **77**, 1945–1960.
- Montelli, R., Nolet, G., Masters, G., Dahlen, F.A. & Hung, S.-H., 2004. Global P and PP traveltime tomography: rays versus waves, *Geophys. J. Int.*, **158**, 637–654.
- Osher, S.J. & Sethian, J.A., 1988. Fronts propagating with curvature dependent speed: algorithms based on Hamilton-Jacobi formulations, *J. Comput. Phys.*, **79**, 12–49.
- Qian, J. & Leung, S., 2004. A level set based Eulerian method for paraxial multivalued traveltimes, *J. Comput. Phys.*, **197**, 711–736.
- Qian, J., Zhang, Y.-T. & Zhao, H.-K., 2007a. Fast sweeping methods for eikonal equations on triangulated meshes, *SIAM J. Numer. Anal.*, **45**, 83–107.
- Qian, J., Zhang, Y.-T. & Zhao, H.-K., 2007b. Fast sweeping methods for static Hamilton-Jacobi equations triangulated meshes, *J. Sci. Comp.*, **31**, 237–271.
- Rawlinson, N., Houseman, G. & Collins, C., 2001. Inversion of seismic refraction and wide-angle reflection traveltime for 3-D layered crustal structure, *Geophys. J. Int.*, **145**, 381–401.
- Sei, A. & Symes, W.W., 1994. Gradient calculation of the traveltime cost function without ray tracing, in *Proceedings of the 65th Ann. Internat. Mtg., Soc. Expl. Geophys.*, Expanded Abstracts, Soc. Expl. Geophys., Tulsa, OK, pp. 1351–1354.
- Sei, A. & Symes, W.W., 1995. Convergent finite-difference traveltime gradient for tomography, in *Proceedings of the 66th Ann. Internat. Mtg., Soc. Expl. Geophys.*, Expanded Abstracts, Soc. Expl. Geophys., Tulsa, OK, pp. 1258–1261.
- Taillandier, C., Noble, M., Chauris, H. & Calandra, H., 2009. First-arrival traveltime tomography based on the adjoint-state method, *Geophysics*, **74**, WCB1–WCB10.
- Tsai, R., Cheng, L.-T., Osher, S.J. & Zhao, H.K., 2003. Fast sweeping method for a class of Hamilton-Jacobi equations, *SIAM J. Numer. Anal.*, **41**, 673–694.
- Washbourne, J. K., Rector, J.W. & Bube, K.P., 2002. Crosswell traveltime tomography in three dimensions, *Geophysics*, **67**, 853–871.
- White, D., 1989. Two-dimensional seismic refraction tomography, *Geophys. J. Int.*, **97**, 223–245.
- Williamson, P., 1990. Tomographic inversion in reflection seismology, *Geophys. J. Int.*, **100**, 255–274.
- Zelt, C., 1999. Modelling strategies and model assessment for wide-angle seismic traveltime data, *Geophys. J. Int.*, **139**, 183–204.
- Zelt, C. & Smith, R., 1992. Seismic traveltime inversion for 2-D crustal velocity structure, *Geophys. J. Int.*, **108**, 16–34.
- Zhao, H.K., 2005. Fast sweeping method for eikonal equations, *Math. Comp.*, **74**, 603–627.
- Zheglouva, P., Farquharson, C. & Hurich, C., 2013. 2D reconstruction of boundaries with level set inversion of travel times, *Geophys. J. Int.*, **192**, 688–698.

APPENDIX A: DERIVATION OF PERTURBATION RELATIONS (15) AND (16)

Consider the eikonal eq. (1) which is valid for both $T_t(\phi + \epsilon \cdot v\tilde{\phi}, S_1 + \epsilon\tilde{S}_1, S_2 + \epsilon\tilde{S}_2)$ and $T_t(\phi, S_1, S_2)$,

$$\begin{aligned} & [\nabla T_t(\phi + \epsilon \cdot v\tilde{\phi}, S_1 + \epsilon\tilde{S}_1, S_2 + \epsilon\tilde{S}_2)]^2 \\ &= S^2(\phi + \epsilon \cdot v\tilde{\phi}, S_1 + \epsilon\tilde{S}_1, S_2 + \epsilon\tilde{S}_2), \end{aligned} \quad (\text{A1})$$

$$[\nabla T_t(\phi, S_1, S_2)]^2 = S^2(\phi, S_1, S_2). \quad (\text{A2})$$

Plugging formula (13) into (A1) and subtracting (A2) from (A1), we get

$$\begin{aligned} 2\epsilon \nabla T_t \cdot \nabla \tilde{T}_t + O(\epsilon^2) &= S^2(\phi + \epsilon \cdot v\tilde{\phi}, S_1 + \epsilon\tilde{S}_1, S_2 + \epsilon\tilde{S}_2) \\ &\quad - S^2(\phi, S_1, S_2). \end{aligned} \quad (\text{A3})$$

From (8) and (9), we have

$$\begin{aligned} & S(\phi + \epsilon \cdot v\tilde{\phi}, S_1 + \epsilon\tilde{S}_1, S_2 + \epsilon\tilde{S}_2) \\ &= S(\phi, S_1, S_2) + \epsilon \cdot v\tilde{\phi} \cdot \frac{S_2 - S_1}{2\tau \cdot \cosh^2 \frac{\phi}{\tau}} + \epsilon\tilde{S}_1 \\ &\quad \cdot [1 - H_\tau(\phi)] + \epsilon\tilde{S}_2 \cdot H_\tau(\phi) + O(\epsilon^2). \end{aligned} \quad (\text{A4})$$

Now, substituting (A4) into (A3), we obtain

$$\begin{aligned} & 2\epsilon \nabla T_t \cdot \nabla \tilde{T}_t + O(\epsilon^2) \\ &= 2\epsilon \cdot S(\phi, S_1, S_2) \cdot \left\{ v\tilde{\phi} \cdot \frac{S_2 - S_1}{2\tau \cdot \cosh^2 \frac{\phi}{\tau}} + \tilde{S}_1 \right. \\ &\quad \left. \cdot [1 - H_\tau(\phi)] + \tilde{S}_2 \cdot H_\tau(\phi) \right\} + O(\epsilon^2). \end{aligned} \quad (\text{A5})$$

To simplify the notation, we denote

$$A(\phi, S_1, S_2) = S(\phi, S_1, S_2) \cdot \frac{S_2 - S_1}{2\tau \cdot \cosh^2 \frac{\phi}{\tau}},$$

$$B(\phi, S_1, S_2) = S(\phi, S_1, S_2) \cdot [1 - H_\tau(\phi)],$$

$$C(\phi, S_1, S_2) = S(\phi, S_1, S_2) \cdot H_\tau(\phi).$$

Then, matching $O(\epsilon)$ terms in (A5), we obtain

$$\begin{aligned} & v\tilde{\phi} \cdot A(\phi, S_1, S_2) + \tilde{S}_1 \cdot B(\phi, S_1, S_2) \\ &+ \tilde{S}_2 \cdot C(\phi, S_1, S_2) - \nabla T_t \cdot \nabla \tilde{T}_t = 0, \end{aligned}$$

which is (15).

Performing a similar calculation for T_r in the domain Ω_1 , we have the relation between $\tilde{\phi}$, \tilde{S}_1 , \tilde{S}_2 and \tilde{T}_r ,

$$\begin{aligned} & v\tilde{\phi} \cdot A(\phi, S_1, S_2) + \tilde{S}_1 \cdot B(\phi, S_1, S_2) \\ &+ \tilde{S}_2 \cdot C(\phi, S_1, S_2) - \nabla T_r \cdot \nabla \tilde{T}_r = 0, \end{aligned}$$

which gives (16).

**APPENDIX B: PROOFS OF LEMMA 3.1
AND LEMMA 3.2**
B1 Derivation of Lemma 3.1

Multiplying (15) by λ , integrating it over Ω and adding to (20), we get

$$\begin{aligned} \frac{\delta E}{\epsilon} &= \int_{\Gamma_1} \tilde{T}_r(T_r - T_r^*) ds + \int_{\Gamma_2} \tilde{T}_t(T_t - T_t^*) ds \\ &\quad + \int_{\Omega} \lambda(W - \nabla T_t \cdot \nabla \tilde{T}_t) dx + O(\epsilon) \\ &= \int_{\Gamma_1} \tilde{T}_r(T_r - T_r^*) ds + \int_{\Gamma_2} \tilde{T}_t(T_t - T_t^*) ds + \int_{\Omega} \lambda W dx \\ &\quad + \int_{\Omega} \operatorname{div}(\lambda \nabla T_t) \cdot \tilde{T}_t dx - \int_{\partial\Omega} \lambda \frac{\partial T_t}{\partial \mathbf{n}} \cdot \tilde{T}_t ds + O(\epsilon), \quad (\text{B1}) \end{aligned}$$

where W is the abbreviation in formula (21) and \mathbf{n} denotes the unit outward normal of $\partial\Omega$. From (B1), we conclude that if λ satisfies the adjoint state eqs (22), (23) and (24) given in Lemma 3.1, the perturbation of the mismatch functional reduces to

$$\frac{\delta E}{\epsilon} = \int_{\Omega} \lambda W dx + \int_{\Gamma_1} \tilde{T}_r(T_r - T_r^*) ds + O(\epsilon),$$

which is (25) in Lemma 3.1.

B2 Derivation of Lemma 3.2

We want to eliminate the term \tilde{T}_r in δE by using (16) as a constraint. We have

$$\begin{aligned} \frac{\delta E}{\epsilon} &= \int_{\Omega} \lambda W dx + \int_{\Gamma_1} \tilde{T}_r(T_r - T_r^*) ds \\ &\quad + \int_{\Omega_1} \mu(W - \nabla T_r \cdot \nabla \tilde{T}_r) dx + O(\epsilon) \\ &= \int_{\Omega} \lambda W dx + \int_{\Gamma_1} \tilde{T}_r(T_r - T_r^*) ds + \int_{\Omega_1} \mu W dx \\ &\quad + \int_{\Omega_1} \operatorname{div}(\mu \nabla T_r) \cdot \tilde{T}_r dx - \int_{\partial\Omega_1} \mu \frac{\partial T_r}{\partial \mathbf{n}} \cdot \tilde{T}_r ds + O(\epsilon). \quad (\text{B2}) \end{aligned}$$

First we consider the adjoint state eqs (26)–(28) given in Lemma 3.2,

$$-\operatorname{div}(\mu \nabla T_r) = 0, \quad \text{in } \Omega_1$$

$$\mu \frac{\partial T_r}{\partial \mathbf{n}} = T_r - T_r^*, \quad \text{on } \Gamma_1$$

$$\mu = 0, \quad \text{on } \partial\Omega_1 \setminus (R \cup \Gamma_1),$$

so that (B2) reduces to

$$\frac{\delta E}{\epsilon} = \int_{\Omega} \lambda W dx + \int_{\Omega_1} \mu W dx - \int_R \mu \frac{\partial T_r}{\partial \mathbf{n}} \cdot \tilde{T}_r ds + O(\epsilon). \quad (\text{B3})$$

To eliminate \tilde{T}_r on R , we use the important relation between T_t and T_r given by (4). Since $T_r(\mathbf{x}) = T_t(\mathbf{x})$ on R , we have

$$\tilde{T}_r(\mathbf{x}) = \tilde{T}_t(\mathbf{x}), \quad \mathbf{x} \text{ on } R. \quad (\text{B4})$$

Substituting (B4) into (B3), we get

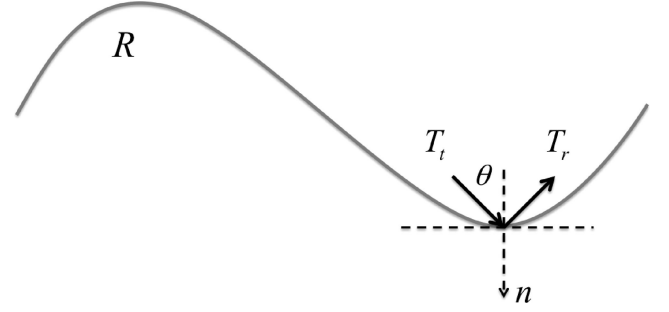


Figure B1. Notation used in simplifying the boundary condition (B8).

$$\frac{\delta E}{\epsilon} = \int_{\Omega} \lambda W dx + \int_{\Omega_1} \mu W dx - \int_R \mu \frac{\partial T_r}{\partial \mathbf{n}} \cdot \tilde{T}_t ds + O(\epsilon). \quad (\text{B5})$$

One finds that the relation (15) can be utilized again to reduce the integrating term involving \tilde{T}_t . Multiplying (15) by $\hat{\mu}$, integrating it over Ω_1 and adding to (B5), we have

$$\begin{aligned} \frac{\delta E}{\epsilon} &= \int_{\Omega} \lambda W dx + \int_{\Omega_1} \mu W dx - \int_R \mu \frac{\partial T_r}{\partial \mathbf{n}} \cdot \tilde{T}_t ds \\ &\quad + \int_{\Omega_1} \hat{\mu}(W - \nabla T_t \cdot \nabla \tilde{T}_t) dx + O(\epsilon) \\ &= \int_{\Omega} \lambda W dx + \int_{\Omega_1} \mu W dx - \int_R \mu \frac{\partial T_r}{\partial \mathbf{n}} \cdot \tilde{T}_t ds + \int_{\Omega_1} \hat{\mu} W dx \\ &\quad + \int_{\Omega_1} \operatorname{div}(\hat{\mu} \nabla T_t) \cdot \tilde{T}_t dx - \int_{\partial\Omega_1} \hat{\mu} \frac{\partial T_t}{\partial \mathbf{n}} \cdot \tilde{T}_t ds + O(\epsilon). \quad (\text{B6}) \end{aligned}$$

Then the adjoint state equation for $\hat{\mu}$ is

$$-\operatorname{div}(\hat{\mu} \nabla T_t) = 0, \quad \text{in } \Omega_1 \quad (\text{B7})$$

$$\hat{\mu} \frac{\partial T_t}{\partial \mathbf{n}} = -\mu \frac{\partial T_r}{\partial \mathbf{n}}, \quad \text{on } R \quad (\text{B8})$$

$$\hat{\mu} = 0, \quad \text{on } \partial\Omega_1 \setminus R, \quad (\text{B9})$$

where (B7) is (29) and (B9) is (31) in Lemma 3.2. Therefore, the mismatch functional finally reduces to (32),

$$\frac{\delta E}{\epsilon} = \int_{\Omega} \lambda W dx + \int_{\Omega_1} (\mu + \hat{\mu}) W dx + O(\epsilon).$$

We can further simplify the boundary condition (B8) in the adjoint state equation for $\hat{\mu}$. As shown in Fig. B1, we have $|\nabla T_t(\mathbf{x})| = |\nabla T_r(\mathbf{x})| = S(\mathbf{x})$ at the point $\mathbf{x} \in R$ due to the eikonal equation. Hence,

$$\frac{\partial T_t}{\partial \mathbf{n}} = \nabla T_t \cdot \mathbf{n} = |\nabla T_t| \cdot |\mathbf{n}| \cdot \cos \theta = S(\mathbf{x}) \cdot \cos \theta$$

$$\frac{\partial T_r}{\partial \mathbf{n}} = \nabla T_r \cdot \mathbf{n} = |\nabla T_r| \cdot |\mathbf{n}| \cdot \cos(\pi - \theta) = -S(\mathbf{x}) \cdot \cos \theta,$$

which imply that

$$\frac{\partial T_t}{\partial \mathbf{n}} = -\frac{\partial T_r}{\partial \mathbf{n}}. \quad (\text{B10})$$

Plugging (B10) into (B8), we finally obtain the simplified boundary condition (30) given by

$$\hat{\mu} = \mu, \quad \text{on } R.$$